Journal pre-proof

DOI: 10.1016/j.cell.2020.04.031

Title: Structural Basis for Potent Neutralization of Betacoronaviruses by Single-domain Camelid Antibodies

Authors: Daniel Wrapp[1#], Dorien De Vlieger[2,3,4#], Kizzmekia S. Corbett[5], Gretel M. Torres[6], Nianshuang Wang[1], Wander Van Breedam[2,3], Kenny Roose[2,3], Loes van Schie[2,3], VIB-CMB COVID-19 Response Team, Markus Hoffmann[7], Stefan Pöhlmann[7,8], Barney S. Graham[5], Nico Callewaert[2,3], Bert Schepens[2,3,4]*, Xavier Saelens[2,3,4]* and Jason S. McLellan[1]*†

Affiliations:

[1] Department of Molecular Biosciences, The University of Texas at Austin, Austin, Texas, USA 78712

[2] VIB-UGent Center for Medical Biotechnology, VIB, 9052 Ghent, Belgium

[3] Department of Biochemistry and Microbiology, Ghent University, 9052 Ghent, Belgium

[4] Department of Biomedical Molecular Biology, Ghent University, 9052 Ghent, Belgium

[5] Vaccine Research Center, National Institute of Allergy and Infectious Diseases, National Institutes of Health, Bethesda, Maryland, USA 20892

[6] Department of Microbiology and Immunology, Geisel School of Medicine at Dartmouth, Lebanon, New Hampshire, USA 03756

[7] Infection Biology Unit, German Primate Center – Leibniz Institute for Primate Research, 37077 Göttingen, Germany

[8]Faculty of Biology and Psychology, University Göttingen, 37077 Göttingen, Germany

[#]These authors contributed equally to this work

*Correspondence: bert.schepens@vib-ugent.be (B.S.), xavier.saelens@vib-ugent.be (X.S.), jmclellan@austin.utexas.edu (J.S.M.)

†Lead contact

SUMMARY

Coronaviruses make use of a large envelope protein called spike (S) to engage host cell receptors and catalyze membrane fusion. Because of the vital role that these S proteins play, they represent a vulnerable target for the development of therapeutics. Here, we describe the isolation of single-domain antibodies (VHHs) from a llama immunized with prefusion-stabilized coronavirus spikes. These VHHs neutralize MERS-CoV or SARS-CoV-1 S pseudotyped viruses, respectively. Crystal structures of these VHHs bound to their respective viral targets reveal two distinct epitopes, but both VHHs interfere with receptor binding. We also show cross-reactivity between the SARS-CoV-1 S-directed VHH and SARS-CoV-2 S, and demonstrate that this cross-reactive VHH neutralizes SARS-CoV-2 S pseudotyped viruses as a bivalent human IgG Fc-fusion. These data provide a molecular basis for the neutralization of pathogenic betacoronaviruses by VHHs and suggest that these molecules may serve as useful therapeutics during coronavirus outbreaks.

INTRODUCTION

Coronaviruses are enveloped, positive-sense RNA viruses that are divided into four genera (α, β, γ, δ) and infect a wide variety of host organisms (Woo et al., 2009). There are at least seven coronaviruses that can cause disease in humans, and four of these viruses (HCoV-HKU1, HCoV-OC43, HCoV-NL63 and HCoV-229E) circulate seasonally throughout the global population, causing mild respiratory disease in most patients (Gaunt et al., 2010). The three remaining viruses, SARS-CoV-1, MERS-CoV and SARS-CoV-2, are zoonotic pathogens that have caused epidemics or pandemics with severe and often fatal symptoms after emerging into the human population (Chan et al., 2020; Huang et al., 2020; Ksiazek et al., 2003; Lu et al., 2020; Zaki et al., 2012). For these highly pathogenic betacoronaviruses, prophylactic and therapeutic interventions are needed.

The surfaces of coronaviruses are decorated with a spike glycoprotein (S), a large class I fusion protein (Bosch et al., 2003). The S protein forms a trimeric complex that can be functionally categorized into two distinct subunits, S1 and S2, that are separated by a protease cleavage site. The S1 subunit contains the receptor-binding domain (RBD), which interacts with a host-cell receptor protein to trigger membrane fusion. The S2 subunit contains the membrane fusion machinery, including the hydrophobic fusion peptide and the α-helical heptad repeats. The functional host cell receptors for SARS-CoV-1 and MERS-CoV are angiotensin converting enzyme 2 (ACE2) and dipeptidyl peptidase 4 (DPP4), respectively (Li et al., 2003; Raj et al., 2013). The interactions between these receptors and their respective RBDs have been thoroughly characterized, both structurally and biophysically (Li et al., 2005; Wang et al., 2013). Recently, it has been reported that SARS-CoV-2 S also makes use of ACE2 as a functional host-cell receptor

and several structures of this complex have already been reported (Hoffmann, 2020; Lan, 2020; Wan et al., 2020; Yan, 2020; Zhou et al., 2020).

Recent advances in cryo-EM have allowed researchers to determine high-resolution structures of the trimeric spike protein ectodomains and understand how S functions as a macromolecular machine (Kirchdoerfer et al., 2016; Li et al., 2005; Walls et al., 2016; Wang et al., 2013). Initial cryo-EM characterization of the SARS-CoV-1 spike revealed that the RBDs adopted at least two distinct conformations. In the "up" conformation, the RBDs jut out away from the rest of S, such that they can easily engage ACE2 without steric clash. In the "down" conformation, the RBDs are tightly packed against the top of the S2 subunit, preventing binding by ACE2 (Gui et al., 2017). Subsequent experiments have corroborated this phenomenon and similar dynamics have been observed in MERS-CoV S, SARS-CoV-2 S and in alphacoronavirus S proteins (Kirchdoerfer et al., 2018; Pallesen et al., 2017; Walls, 2020; Wrapp and McLellan, 2019; Wrapp et al., 2020; Yuan et al., 2017). Due to the relatively low abundance of particles that can be observed by cryo-EM with three RBDs in the up conformation, it is thought that this conformation may correspond to an energetically unstable state (Kirchdoerfer et al., 2018; Pallesen et al., 2017). These observations have led to the hypothesis that the CoV RBDs might act as a molecular ratchet: a receptor-binding event would trap the RBD in the less stable up conformation, leading to gradual destabilization of S1 until S2 is finally triggered to initiate membrane fusion. Recent experiments characterizing RBD-directed anti-SARS-CoV-1 antibodies that trap the SARS-CoV-1 RBD in the up conformation and lead to destabilization of the prefusion spike have lent support to this hypothesis (Walls et al., 2019).

Numerous anti-SARS-CoV-1 RBD and anti-MERS-CoV RBD antibodies have been reported and their mechanisms of neutralization can be attributed to the occlusion of the

receptor-binding site and to trapping the RBD in the unstable up conformation, effectively acting as a receptor mimic that triggers a premature transition from the prefusion-to-postfusion conformation (Hwang et al., 2006; Walls et al., 2019; Wang et al., 2018; Wang et al., 2015). In addition to conventional antibodies, camelids also produce heavy chain-only antibodies (HCAbs), which contain a single variable domain (VHH) instead of two variable domains (VH and VL) that make up the equivalent antigen-binding fragment (Fab) of conventional IgG antibodies (Hamers-Casterman et al., 1993). This single variable domain, in the absence of an effector domain, is referred to as a single-domain antibody, VHH or Nanobody® and typically can acquire affinities and specificities for antigens comparable to conventional antibodies. VHHs can easily be constructed into multivalent formats and they have higher thermal stability and chemostability than most antibodies (De Vlieger et al., 2018; Dumoulin et al., 2002; Govaert et al., 2012; Laursen et al., 2018; Rotman et al., 2015; van der Linden et al., 1999). VHHs are also known to be less susceptible to steric hindrances that might prevent the binding of larger conventional antibodies (Forsman et al., 2008). Their advantageous biophysical properties have led to the evaluation of several VHHs as therapeutics against common respiratory pathogens, such as respiratory syncytial virus (RSV) (Detalle et al., 2016; Rossey et al., 2017). The use of VHHs as biologics in the context of a respiratory infection is a particularly attractive application, since the highly stable VHHs can be nebulized and administered via an inhaler directly to the site of infection (Respaud et al., 2015). Moreover, due to their stability after prolonged storage, VHHs could be stockpiled as therapeutic treatment options in case of an epidemic. Although therapeutics against MERS-CoV and SARS-CoV-2 are sorely needed, the feasibility of using VHHs for this purpose has not yet been adequately explored. Several MERS-CoV S-directed VHHs have been reported as a result of camelid immunization, but their epitopes remain largely

undefined, other than being classified as RBD-directed (Stalin Raj et al., 2018; Zhao et al., 2018).

Here we report the isolation of two potently neutralizing VHHs directed against the SARS-CoV-1 and MERS-CoV RBDs, respectively. These VHHs were elicited in response to immunization of a llama with prefusion-stabilized SARS-CoV-1 and MERS-CoV S proteins. We solved the crystal structures of these two VHHs in complex with their respective viral epitopes which suggested likely mechanisms of neutralization were occlusion of the receptor binding interface and trapping of the RBDs in the up conformation. We also show that the SARS-CoV-1 RBD-directed VHH cross-reacts with the SARS-CoV-2 RBD and can block the receptor-binding interface. After engineering this VHH into a bivalent Fc-fusion, we show that this cross-reactive VHH can also neutralize SARS-CoV-2 S bearing pseudoviruses. We further demonstrate that the VHH-Fc fusion can be produced at high yields in an industry-standard CHO cell system, suggesting that it merits further investigation as a potential therapeutic for the ongoing COVID-19 pandemic.

RESULTS

Isolation of betacoronavirus S-directed VHHs

Our initial aim was to isolate VHHs that could potently neutralize MERS-CoV and SARS-CoV-1. Therefore, we sequentially immunized a llama subcutaneously twice with SARS-CoV-1 S protein, twice with MERS-CoV S protein, once again with SARS-CoV-1 S and finally with both SARS-CoV-1 and MERS-CoV S protein (**S. Figure 1A**). To obtain VHHs directed against these spike proteins, two consecutive rounds of panning were performed by phage display using either SARS-CoV-1 S or MERS-CoV S protein. Positive clones were sequenced and multiple sequence

alignment and phylogenetic analysis using the neighbor-joining method revealed that seven unique MERS-CoV S and five unique SARS-CoV-1 S VHHs were isolated (**S. Figure 1B**). These VHHs and an irrelevant control (RSV F-VHH, directed against the F protein of human respiratory syncytial virus) were subsequently expressed in *Pichia pastoris* and purified from the yeast medium (Rossey et al., 2017). The binding of the purified VHHs to prefusion-stabilized MERS-CoV S and SARS-CoV-1 S was confirmed by ELISA (**S. Figure 1C**). As expected, the irrelevant control had no detectable binding to MERS-CoV S and SARS-CoV-1 S. Four clones (MERS VHH-55, -12, -34 and -40), obtained after panning on MERS-CoV S protein, bound with high affinity to prefusion-stabilized MERS-CoV S, whereas the affinities of VHH-2, -20 and -15 were 100- to 1000-fold weaker. Of the five clones isolated after panning on SARS-CoV-1 S protein, three VHH clones (SARS VHH-72, -1 and -6) interacted strongly with prefusion stabilized SARS-CoV-1 S protein. We observed no cross-reactivity of MERS VHHs with SARS-CoV-1 S and vice versa (data not shown).

VHHs neutralize coronavirus S pseudotyped viruses

To assess the antiviral activity of the MERS-CoV and SARS-CoV S-directed VHHs, we performed *in vitro* neutralization assays using MERS-CoV England1 S and SARS-CoV-1 Urbani S pseudotyped lentiviruses. The high affinity MERS VHH-55, -12, -34 and -40 neutralized MERS-CoV S pseudotyped virus with IC_{50} values ranging from 0.014 to 2.9 µg/mL (0.9 nM to 193.3 nM), while the lower affinity MERS-CoV or SARS-CoV-1 specific VHHs had no inhibitory effect (**S. Table 1**). SARS VHH-72 and -44 neutralized lentiviruses pseudotyped with SARS-CoV-1 S with IC_{50} values of 0.14 (9 nM) and 5.5 µg/mL (355 nM), respectively. No binding was observed for SARS VHH-44 to prefusion stabilized SARS-CoV-1 S protein in the ELISA assay. Sequence analysis revealed that the neutralizing MERS-CoV specific VHHs -12, -

40 and -55 have highly similar complementarity-determining regions (CDRs), indicating that they likely belong to the same clonal family, and may bind to the same epitope (**S. Figure 2**). In contrast, the CDRs from the SARS-CoV S-specific VHHs -44 and -72 are very different.

Mapping domain-specificity of betacoronavirus S-directed VHHs

To map the epitopes targeted by the neutralizing VHHs, we tested binding to recombinant MERS-CoV S1, RBD, and N-terminal domain (NTD) and SARS-CoV-1 RBD and NTD by ELISA (**Figure 1A and S. Figure 3**).The MERS-CoV S-specific VHHs strongly bound to MERS-CoV S1 and RBD in a concentration-dependent manner, and failed to bind to the MERS-CoV NTD. Similarly, strong binding of SARS VHH-72 to the SARS-CoV-1 RBD protein but not the SARS-CoV-1 NTD protein was observed. No binding of SARS VHH-44 to either the SARS-CoV-1 S or NTD protein was detected, leaving the domain that this VHH recognizes undetermined. These data demonstrate that the neutralizing SARS VHH-72 and MERS VHH-55 target the RBDs. Based on the specificity and potent neutralizing capacity of SARS VHH-72 and MERS VHH-55, we measured the affinities of these VHHs by immobilizing recombinantly expressed VHH to an SPR sensorchip and determined the binding kinetics for their respective RBDs. We found that both of these VHHs bound to their targets with high affinity. SARS VHH-72 bound to its target with an affinity of 1.2 nM and MERS VHH-55 bound to its target with an affinity of 79.2 pM, in part due to a very slow off-rate constant (k_d = 8.2 x10^{-5} s^{-1}) (**Figure 1B**).

Structural basis of VHH interaction with RBDs

To investigate the molecular determinants that mediate potent neutralization and high-affinity binding by MERS VHH-55, we solved the crystal structure of MERS VHH-55 bound to the MERS-CoV RBD. Crystals grew in space group $C222_1$ and diffracted X-rays to a resolution of 3.4 Å. After determining a molecular replacement solution and iterative building and refinement,

our structure reached an R_{work}/R_{free} of 24.7%/27.8% (**S. Table 2**). The asymmetric unit of this crystal contained eight copies of the MERS VHH-55 + MERS-CoV RBD complex and had a solvent content of ~58%. The electron density allowed unambiguous definition of the interface between the RBD and VHH, with the three CDRs forming extensive binding contacts with the RBD, burying 716 $Å^2$ of surface area by pinching the RBD between the CDR2 and CDR3. The CDR3 of MERS VHH-55 is looped over the DPP4-binding interface, occluding DPP4 from productively engaging the MERS-CoV RBD (**Figure 2A-B**).

There are numerous contacts between the CDRs of MERS VHH-55 and the MERS-CoV RBD; most are confined to CDRs 2 and 3. A network of interactions from all three CDRs (**Figure 2C-D**) suggests that RBD residue Arg542 has a critical role in MERS VHH-55 binding. This arginine has previously been identified as one of the twelve conserved residues that are crucial for high-affinity DPP4 engagement (**S. Figure 4A**) (Wang et al., 2013; Wang et al., 2014).

In addition to forming a salt bridge with Glu513 from the MERS-CoV RBD, Trp99 of the MERS VHH-55 CDR3 is positioned near a hydrophobic patch formed by Phe506 (**S. Figure 4B**). This residue exhibits natural sequence variation in several MERS-CoV strains, such that a Leu is occasionally observed at this position. To evaluate the extent to which this substitution impacts MERS VHH-55 binding, we generated a F506L substitution and measured binding by SPR (**S. Figure 4C**). This substitution resulted in a ~200-fold reduction in MERS VHH-55 binding affinity. Despite this substantial reduction, the affinity of MERS VHH-55 to MERS-CoV RBD F506L remained high, with a K_D = 16.5 nM. Other than the variability that is observed at position 506 of the MERS-CoV RBD, the rest of the MERS VHH-55 epitope is highly conserved across the 863 strains that are curated in the MERS-CoV Virus Variation database (**S. Figure**

4A). Despite this predicted broad recognition of MERS-CoV strains, the average sequence identity of 24% between the MERS-CoV RBD and the RBDs from the seasonal coronaviruses HCoV-HKU1, HCoV-OC43, HCoV-229E and HCoV-NL63, makes it unlikely that MERS VHH-55 would cross-react with any of these more distantly related spike proteins.

We also sought to discover the molecular determinants of binding between SARS VHH-72 and the SARS-CoV-1 RBD by determining the crystal structure of this complex. Crystals grew in space group $P3_121$ and diffracted X-rays to a resolution of 2.2 Å. We obtained a molecular replacement solution and refined the structure to an R_{work}/R_{free} of 20.3%/23.6% through iterative building and refinement (**S. Table 2**). Our structure reveals that CDRs 2 and 3 contribute to most of the 834 $Å^2$ of buried surface area at the binding interface (**Figure 3A**). This epitope does not, however, overlap with the ACE2 footprint on the SARS-CoV-1 RBD. Rather, ACE2 would clash with the CDR-distal framework of SARS VHH-72, as opposed to classical receptor-blocking in which the CDRs would occupy the ACE2 binding interface (**Figure 3B**). ACE2 also carries an *N*-glycan modification at position Asn322 (Yan, 2020). When bound to the RBD, this *N*-glycan points into the space that is occupied by SARS VHH-72, forming an even larger clash (**Figure 3C**). SARS VHH-72 binds to the SARS-CoV-1 RBD through a hydrogen-bond network involving CDRs 2 and 3, in which backbone groups participate extensively (**Figure3D-E**). This network probably accounts for the high-affinity binding that we observed for these two molecules.

SARS VHH-72 cross-reacts with WIV1-CoV and SARS-CoV-2

Analysis of 10 available SARS-CoV-1 sequences revealed a high degree of conservation in the residues that make up the SARS VHH-72 epitope, prompting us to explore the breadth of SARS

VHH-72 binding (**S. Figure 5A**). WIV1-CoV is a betacoronavirus found in bats that is closely related to SARS-CoV-1 and also utilizes ACE2 as a host-cell receptor (Ge et al., 2013). Due to the relatively high degree of sequence conservation between SARS-CoV-1 and WIV1-CoV, we expressed the WIV1-CoV RBD and measured binding to SARS VHH-72 by SPR (**S. Figure 5B**). SARS VHH-72 exhibited high-affinity binding to the WIV1-CoV RBD (7.4 nM), demonstrating that it cross-reacts with these two closely related coronaviruses (**S. Figure 5C**).

Based on the high degree of structural homology that has been reported between SARS-CoV-1 S and SARS-CoV-2 S (Walls, 2020; Wrapp et al., 2020), we also tested SARS VHH-72 for cross-reactivity against the SARS-CoV-2 RBD and subdomain 1 (SARS-CoV-2 RBD-SD1) by SPR (**Figure 4**). The equilibrium dissociation constant of SARS VHH-72 for the SARS-CoV-2 RBD-SD1 was ~39 nM, substantially higher than for the SARS-CoV-1 RBD. The weaker binding can primarily be attributed to an increase in the dissociation rate constant (**Figure 4A**). The only variant residue on the SARS-CoV-1 RBD that makes direct contact with SARS VHH-72 is Arg426, which is Asn439 in the SARS-CoV-2 RBD (**Figure 3C**). This mutation prevents the formation of a salt bridge with Asp61 from SARS VHH-72, which likely contributes to the increased dissociation rate constant. Due to an average sequence identity of only 25% between the SARS-CoV-1 RBD and the RBDs of the seasonal coronaviruses, we predict that SARS VHH-72 cross-reactivity is likely confined to the RBD from SARS-CoV-2 and closely related betacoronaviruses such as WIV1-CoV.

VHHs disrupt RBD dynamics and receptor-binding

The RBDs of MERS-CoV S, SARS-CoV-1 S and SARS-CoV-2 S undergo dynamic conformational rearrangements that alternately mask and present their receptor-binding

interfaces and potential neutralizing epitopes to host molecules. By aligning the crystal structures of the MERS VHH-55 and SARS VHH-72 complexes to the cryo-EM structures of the MERS-CoV, SARS-CoV-1 and SARS-CoV-2 spike proteins, we can begin to understand how these molecules might function in the context of these dynamic rearrangements. When the MERS-CoV RBDs are all in the down conformation or all in the up conformation, MERS VHH-55 would be able to bind all three of the protomers making up the functional spike trimer without forming any clashes. However, if a down protomer was bound by MERS VHH-55 and the neighboring protomer sampled the up conformation, this RBD would then be trapped in this state by the presence of the neighboring MERS VHH-55 molecule (**Figure 5A**). This conformational trapping would be even more pronounced upon SARS VHH-72 binding to the SARS-CoV-1 S protein or the SARS-CoV-2 S protein. Due to the binding angle of SARS VHH-72, when a bound SARS-CoV-1 or SARS-CoV-2 RBD samples the down conformation, it would clash with the S2 fusion subunit, regardless of the conformations of the neighboring RBDs (**Figure 5B-C**). Therefore, once a single SARS VHH-72 binding event took place, the bound protomer would be trapped in the up conformation until either SARS VHH-72 was released or until the S protein was triggered to undergo the prefusion-to-postfusion transition. Based on the binding angles of MERS VHH-55 and SARS VHH-72, we can conclude that these molecules would likely disrupt the RBD dynamics in the context of a trimeric S protein by trapping the up conformation. Because this up conformation is unstable and leads to S protein triggering, it is possible that this conformational trapping may at least partially contribute to the neutralization mechanisms of these VHHs.

To investigate the receptor-blocking ability of the VHHs, we performed a BLI-based assay in which the SARS-CoV-1, SARS-CoV-2 and MERS-CoV RBDs were immobilized to

biosensor tips, dipped into VHHs and then dipped into wells containing the recombinant, soluble host cell receptors. We found that when tips coated with the MERS-CoV RBD were dipped into MERS VHH55 before being dipped into DPP4, there was no increase in response that could be attributed to receptor binding. When tips coated with the MERS-CoV RBD were dipped into SARS VHH-72 and then DPP4, a robust response signal was observed, as expected. Similar results were observed when the analogous experiments were performed using the SARS-CoV-1 or SARS-CoV-2 RBDs, SARS VHH-72 and ACE2 (**Figure 5D**). These results are consistent with conclusions from our structural analysis that these VHHs can neutralize their respective viral targets by directly interfering with host-cell receptor binding.

Bivalent SARS VHH-72 neutralizes SARS-CoV-2 S pseudoviruses

Despite the relatively high affinity determined by SPR of SARS VHH-72 for the SARS-CoV-2 RBD, we could not detect the interaction by ELISA. Moreover, SARS VHH-72 did not neutralize SARS-CoV-2 S VSV pseudoviruses, possibly due to the high dissociation rate constant, although it readily neutralized SARS-CoV-1 pseudotyped reporter viruses (**Figure 6A-D**). In an attempt to compensate for this rapid dissociation, we engineered two bivalent variants of SARS VHH-72. These included a tail-to-head fusion of two SARS VHH-72 molecules connected by a $(GGGGS)_3$ linker (VHH-72-VHH-72) and a genetic fusion of SARS VHH-72 to the Fc domain of human IgG1 (VHH-72-Fc) (**S. Figure 6A-C**). These bivalent SARS VHH-72 constructs bound to both prefusion SARS-CoV-1 S and SARS-CoV-2 RBD-SD1 as demonstrated by ELISA and by a dose-dependent reduction in the binding of SARS-CoV-2 RBD-SD1 to the ACE2 receptor on Vero E6 cells (**Figure 6C-D and S. Figure 6B-C**). We also detected binding of both of these constructs to full length SARS-CoV-1 S and SARS-CoV-2 S expressed on the surface of mammalian cells (**S. Figure 6D-E**). Supernatants of HEK 293S cells

transiently transfected with VHH-72-Fc exhibited neutralizing activity against both SARS-CoV-1 and SARS-CoV-2 S VSV pseudoviruses in the same assay which showed no such cross-reactive neutralization for monovalent SARS VHH-72 (**Figure 6E-F**). A BLI experiment measuring binding of VHH-72-Fc to immobilized SARS-CoV-2 RBD-SD1 further confirmed that bivalency was able to compensate for the high dissociation constant of the monomer (**Figure 7A**). Furthermore, the cross-neutralizing VHH-72-Fc construct reached expression levels of ~300 mg/L in ExpiCHO cells (**Figure 7B**). Using VHH-72-Fc purified from ExpiCHO cells and a SARS-CoV-2 S pseudotyped VSV with a luciferase reporter, we evaluated the neutralization capacity of VHH-72-Fc and found that it neutralized pseudovirus with an IC_{50} of approximately 0.2 μg/mL (**Figure 7C**).

DISCUSSION

Here we report the isolation and characterization of two potently neutralizing single-domain antibodies from a llama immunized with prefusion-stabilized MERS-CoV and SARS-CoV-1 spikes. These VHHs bind to the spike RBDs with high affinity and are capable of neutralizing S pseudotyped viruses *in vitro*. To our knowledge, the isolation and characterization of SARS-CoV-1 S-directed VHHs have not been described before. Several MERS-CoV S-specific VHHs have been described, all of which have been directed against the RBD. Several of these VHHs have also been reported to block DPP4 binding, much like MERS VHH-55 (Stalin Raj et al., 2018; Zhao et al., 2018). By solving the crystal structures of these newly isolated VHHs in complex with their respective viral targets, we provide detailed insights into epitope binding and their mechanisms of neutralization.

A number of RBD-directed conventional antibodies have been described that are capable of neutralizing SARS-CoV-1 or MERS-CoV. The epitope of MERS VHH-55 overlaps with the

epitopes of several of these MERS-CoV RBD-directed antibodies including C2, MCA1, m336, JC57-14, D12, 4C2 and MERS-27 (Chen et al., 2017; Li et al., 2015; Wang et al., 2018; Wang et al., 2015; Ying et al., 2015; Yu et al., 2015) (**S. Figure 7A**). The epitope of SARS VHH-72 does not significantly overlap with the epitopes of any previously described antibodies other than that of the recently described CR3022, which can also bind to the RBDs of both SARS-CoV-1 and SARS-CoV-2 S (Hwang et al., 2006; Pak et al., 2009; Prabakaran et al., 2006; Walls et al., 2019; Yuan M, 2020) (**S. Figure 7B**). However, unlike SARS VHH-72, CR3022 does not prevent the binding of ACE2 and it lacks neutralizing activity against SARS-CoV-2 (Tian et al., 2020; Yuan M, 2020). This discrepancy in function, despite the partially overlapping epitope, is likely due to the different angles of approach that these two antibodies adopt (**S. Figure 7C**). Because SARS VHH-72 binds with a nanomolar K_D to a portion of the SARS-CoV-1 S RBD that exhibits low sequence variation, as demonstrated by its cross-reactivity with the WIV1-CoV and SARS-CoV-2 RBDs, it may broadly bind S proteins from other SARS-CoV-like viruses. We show that by engineering a bivalent VHH-72-Fc construct, we can compensate for the relatively high off-rate constant of the monovalent SARS VHH-72. This bivalent molecule expresses well in transiently transfected ExpiCHO cells (~300 mg/L) and can neutralize SARS-CoV-2 S pseudoviruses *in vitro*. Future panning efforts using existing libraries and SARS-CoV-2 S may yield even more potent neutralizers.

Due to the inherent thermostability and chemostability of VHHs, they have been investigated as potential therapeutics against several diseases. Several HIV- and influenza-directed VHHs have been reported previously, and there are multiple RSV-directed VHHs that have been evaluated (Detalle et al., 2016; Ibanez et al., 2011; Koch et al., 2017; Rossey et al., 2017). The possibility of administering these molecules via a nebulized spray is particularly

attractive in the case of respiratory pathogens because the VHHs could theoretically be inhaled directly to the site of infection in an effort to maximize bioavailability and function (Larios Mora et al., 2018). Due to the current lack of treatments for MERS, SARS and COVID-19 and the devastating effects associated with pandemic coronavirus outbreaks, both prophylactic and therapeutic interventions are sorely needed. It is our hope that due to their favorable biophysical properties and their potent neutralization capacity, MERS VHH-55, SARS VHH-72 and VHH-72-Fc may serve as both useful reagents for researchers and as potential therapeutic candidates.

FIGURE LEGENDS

Figure 1: Epitope determination and biophysical characterization of MERS VHH-55 and SARS VHH-72. **A**) Reactivity of MERS-CoV and SARS-CoV RBD-directed VHHs against the MERS-CoV and SARS-CoV-1 RBD, respectively. A VHH against an irrelevant antigen (F-VHH) was included as a control. **B**) SPR sensorgrams showing binding between the MERS-CoV RBD and MERS VHH-55 (*left*) and SARS-CoV-1 RBD and SARS VHH-72 (*right*). Binding curves are colored black and fit of the data to a 1:1 binding model is colored red.

Figure 2: The crystal structure of MERS VHH-55 bound to the MERS-CoV RBD. **A**) MERS VHH-55 is shown as blue ribbons and the MERS-CoV RBD is shown as a tan-colored molecular surface. The DPP4 binding interface on the MERS-CoV RBD is colored red. **B**) The structure of DPP4 bound to the MERS-CoV RBD (PDB: 4L72) is aligned to the crystal structure of MERS VHH-55 bound to the MERS-CoV RBD. A single monomer of DPP4 is shown as a red, transparent molecular surface. **C**) A zoomed-in view of the panel from **2A**, with the MERS-CoV RBD now displayed as tan-colored ribbons. Residues that form interactions are shown as sticks,

with nitrogen atoms colored dark blue and oxygen atoms colored red. Hydrogen-bonds and salt bridges between MERS VHH-55 and the MERS-CoV RBD are shown as black dots. **D**) The same view from **2C** has been turned by approximately 90° to show additional contacts. Residues that form interactions are shown as sticks, with nitrogen atoms colored dark blue and oxygen atoms colored red. Hydrogen-bonds and salt bridges between MERS VHH-55 and the MERS-CoV RBD are shown as black dots.

Figure 3: The crystal structure of SARS VHH-72 bound to the SARS-CoV-1 RBD. **A**) SARS VHH-72 is shown as dark blue ribbons and the SARS-CoV-1 RBD is shown as a pink-colored molecular surface. The ACE2 binding interface on the SARS-CoV-1 RBD is colored red. **B**) The structure of ACE2 bound to the SARS-CoV-1 RBD (PDB: 2AJF) is aligned to the crystal structure of SARS VHH-72 bound to the SARS-CoV-1 RBD. ACE2 is shown as a red, transparent molecular surface. **C**) A simulated *N*-linked glycan containing an energy-minimized trimannosyl core (derived from PDB ID: 1HD4) is modeled as red sticks, coming from Asn322 in ACE2. ACE2 is shown as a red molecular surface, the SARS-CoV-1 RBD is shown as pink ribbons and SARS VHH-72 is shown as a dark blue, transparent molecular surface. **D**) A zoomed-in view of the panel from **3A** is shown, with the SARS-CoV-1 RBD now displayed as pink-colored ribbons. Residues that form interactions are shown as sticks, with nitrogen atoms colored dark blue and oxygen atoms colored red. Hydrogen bonds and salt bridges between SARS VHH-72 and the SARS-CoV-1 RBD are shown as black dots. **E**) The same view from **3D** has been turned by 60° to show additional contacts. Residues that form interactions are shown as sticks, with nitrogen atoms colored dark blue and oxygen atoms colored red. Interactions between SARS VHH-72 and the SARS-CoV-1 RBD are shown as black dots.

Figure 4: SARS VHH-72 cross-reacts with SARS-CoV-2. **A**) An SPR sensorgram measuring the binding of SARS VHH-72 to the SARS-CoV-2 RBD-SD1. Binding curves are colored black and fit of the data to a 1:1 binding model is colored red. **B**) The crystal structure of SARS VHH-72 bound to the SARS-CoV-1 RBD is shown with SARS VHH-72 as dark blue ribbons and the RBD as a pink molecular surface. Amino acids that vary between SARS-CoV-1 and SARS-CoV-2 are colored green.

Figure 5: Neutralizing mechanisms of MERS VHH-55 and SARS VHH-72. **A**) The MERS-CoV spike (PDB ID: 5W9H) is shown as a transparent molecular surface, with each monomer colored either white, gray or tan. Each monomer is bound by MERS VHH-55, shown as blue ribbons. The clash between MERS VHH-55 bound to the white monomer and the neighboring tan RBD is highlighted by the red ellipse. **B**) The SARS-CoV-1 spike (PDB ID: 5X58) is shown as a transparent molecular surface, with each protomer colored either white, gray or pink. Every monomer is bound by a copy of SARS VHH-72, shown as dark blue ribbons. The clashes between copies of SARS VHH-72 and the two neighboring spike monomers are highlighted by the red circle. **C**) The SARS-CoV-2 spike (PDB ID: 6VXX) is shown as a transparent molecular surface, with each protomer colored either white, gray or green. Every monomer is bound by a copy of SARS VHH-72, shown as dark blue ribbons. The clashes between copies of SARS VHH-72 and the two neighboring spike monomers are highlighted by the red circle. The SARS-CoV-2 trimer appears smaller than SARS-CoV-1 S due to the absence of flexible NTD-distal loops which could not be built during cryo-EM analysis. **D)** CoV VHHs prevent MERS-CoV RBD, SARS-CoV-1 RBD and SARS-CoV-2 RBD-SD1 from interacting with their receptors.

366 The results of the BLI-based receptor-blocking experiment are shown. The legend lists the
367 immobilized RBDs and the VHHs or receptors that correspond to each curve.
368
369 **Figure 6**: SARS VHH-72 bivalency permits SARS-CoV-2 pseudovirus neutralization. **A**)
370 SARS-CoV-1 S and **B**) SARS-CoV-2 S VSV pseudoviruses were used to evaluate the
371 neutralization capacity of SARS VHH-72. MERS VHH-55 and PBS were included as negative
372 controls. Luciferase activity is reported in counts per second (c.p.s.). NI, cells were not infected.
373 **C**) Binding of bivalent VHHs was tested by ELISA against SARS-CoV-1 S and **D**) SARS-CoV-
374 2 RBD-SD1. VHH-72-Fc refers to SARS VHH-72 fused to a human IgG1 Fc domain by a
375 $GS(GGGGS)_2$ linker. VHH-72-Fc (S) is the same Fc fusion with a GS, rather than a
376 $GS(GGGGS)_2$, linker. GBP is an irrelevant GFP-binding protein. VHH-72-VHH-72 refers to the
377 tail-to-head construct with two SARS VHH-72 proteins connected by a $(GGGGS)_3$ linker. VHH-
378 23-VHH-23 refers to the two irrelevant VHHs linked via the same $(GGGGS)_3$ linker. **E**) SARS-
379 CoV-1 S and **F**) SARS-CoV-2 S pseudoviruses were used to evaluate the neutralization capacity
380 of bivalent VHH-72-Fc. GBP and PBS were included as negative controls. NI, cells were not
381 infected.
382
383 **Figure 7**: VHH-72-Fc neutralizes SARS-CoV-2 S pseudoviruses. **A**) BLI sensorgram measuring
384 apparent binding affinity of VHH-72-Fc to immobilized SARS-CoV-2 RBD-Fc. Binding curves
385 are colored black, buffer-only blanks are colored gray and the fit of the data to a 1:1 binding
386 curve is colored red. **B**) Time course analysis of VHH-72-Fc expression in ExpiCHO cells. Cell
387 culture supernatants of transiently transfected ExpiCHO cells were removed on days 3-7 after
388 transfection (or until cell viability dropped below 75%), as indicated. Two control mAbs were

included for comparison, along with the indicated amounts of purified GBP-Fc as a loading control. **C**) SARS-CoV-2 S pseudotyped VSV neutralization assay. Monolayers of Vero E6 cells were infected with pseudoviruses that had been pre-incubated with the mixtures indicated by the legend. The VHH-72-Fc used in this assay was purified after expression in ExpiCHO cells (n = 4). VHH-23-Fc is an irrelevant control VHH-Fc (n = 3). NI, cells were not infected. Luciferase activity is reported in counts per second (c.p.s.) ± SEM.

SUPPLEMENTAL FIGURE LEGENDS

Supplementary Figure 1: CoV VHH immunization and panning. Related to Figure 1. **A**) Schematic depicting the immunization strategy that was used to isolate both SARS-CoV-1 S and MERS-CoV S-directed VHHs from a single llama. The prefusion stabilized SARS-CoV-1 spike is shown in pink and the prefusion stabilized MERS-CoV spike is shown in tan. **B**) Phylogenetic tree of the isolated MERS-CoV and SARS-CoV S-directed VHHs, based on the neighbor joining method. **C**) Reactivity of MERS-CoV and SARS-CoV S-directed VHHs with the prefusion stabilized MERS-CoV S and SARS-CoV-1 S protein, respectively. A VHH against an irrelevant antigen (F-VHH) was included as a control.

Supplementary Figure 2: Sequence alignment of neutralizing SARS-CoV and MERS-CoV S-directed VHHs. Related to Figure 1. Invariant residues are shown as black dots. The CDRs are shown in boxes and Kabat numbering is shown above.

Supplementary Figure 3: Lack of binding of MERS-CoV and SARS-CoV directed VHHs to non-RBD epitopes. Related to Figure 1. ELISA data showing binding of the MERS-CoV specific

VHHs to the MERS-CoV S1 protein and absence of binding of the MERS-CoV and SARS-CoV specific VHHs against the MERS-CoV NTD and SARS-CoV-1 NTD, respectively. A VHH against an irrelevant antigen (F-VHH) was included as a control.

Supplementary Figure 4: MERS VHH-55 binds to a relatively conserved epitope on the MERS-CoV RBD. Related to Figure 2. A) The crystal structure of MERS VHH-55 bound to the MERS-CoV RBD is shown with MERS VHH-55 in white ribbons and the MERS-CoV RBD as a multicolored molecular surface. More variable residues are shown in warm colors and more conserved residues are shown in cool colors according to the spectrum (*bottom*). Sequence alignments and variability mapping was performed using ConSurf. **B**) The crystal structure of MERS VHH-55 bound to the MERS-CoV RBD is shown as ribbons with MERS VHH-55 colored blue and the MERS-CoV RBD colored tan. Phe506 from the MERS-CoV RBD and Trp99 from MERS VHH-55, which are thought to form hydrophobic interactions with one another are shown as sticks surrounded by a transparent molecular surface. **C**) SPR sensorgram measuring the binding of MERS VHH-55 to the naturally occurring MERS-CoV RBD F506L variant. Binding curves are colored black and the fit of the data to a 1:1 binding model is colored red.

Supplementary Figure 5: SARS VHH-72 binds to a broadly conserved epitope on the SARS-CoV-1 RBD. Related to Figure 3. **A**) The crystal structure of SARS VHH-72 bound to the SARS-CoV-1 RBD is shown, with colors corresponding to those of **SFig 4A**. **B**) The crystal structure of SARS VHH-72 bound to the SARS-CoV-1 RBD is shown with SARS VHH-72 as dark blue ribbons and the RBD as a pink molecular surface. Amino acids that vary between

SARS-CoV-1 and WIV1-CoV are colored teal. **C**) SPR sensorgram measuring the binding of SARS VHH-72 to the WIV1-CoV RBD. Binding curves are colored black and the fit of the data to a 1:1 binding model is colored red.

Supplementary Figure 6: Engineering a functional bivalent VHH construct. Related to Figure 6. **A**) Flow cytometry measuring the binding of the bivalent SARS VHH-72 tail-to-head fusion (VHH-72-VHH-72) to SARS-CoV-1 or SARS-CoV-2 S expressed on the cell surface. VHH-23-VHH-23, a bivalent tail-to-head fusion of an irrelevant nanobody, was included as a negative control. **B**) Binding of SARS-CoV-2 RBD-SD1 to Vero E6 cells is prevented by VHH-72-VHH-72 in a dose-dependent fashion. Binding of SARS-CoV-2 RBD-SD1 to Vero E6 cells was detected by flow cytometry in the presence of the indicated bivalent VHHs (n = 2 except VHH-72-VHH-72 and VHH-23-VHH-23 at 5 μg/ml, n = 5). **C**) Binding of SARS-CoV-2 RBD-SD1 to Vero E6 cells is prevented by bivalent VHH-72-Fc fusion proteins in a dose-dependent fashion. Binding of SARS-CoV-2 RBD-SD1-Fc to Vero E6 cells was detected by flow cytometry in the presence of the indicated constructs and amounts (n = 2 except no RBD, n = 4). **D**) Cell surface binding of SARS VHH-72 to SARS-CoV-1 S. 293T cells were transfected with a GFP expression plasmid together with a SARS-CoV-1 S expression plasmid. Binding of the indicated protein is expressed as the median fluorescent intensity (MFI), measured to detect the His-tagged MERS VHH-55 or SARS VHH-72 or the SARS VHH-72-Fc fusions, of the GFP positive cells divided by the MFI of the GFP negative cells**. E)** Cell surface binding of SARS VHH-72 to SARS-CoV-2. MFI was calculated using the same equation as **S. Figure 6D**.

Supplementary Figure 7: Comparison of the CoV VHH epitopes with known RBD-directed antibodies. Related to Figures 2 and 3. **A**) The structure of MERS VHH-55 bound to the MERS-CoV RBD is shown with MERS VHH-55 as blue ribbons and the MERS-CoV RBD as a white molecular surface. Epitopes from previously reported crystal structures of the MERS-CoV RBD bound by RBD-directed antibodies are shown as colored patches on the MERS-CoV RBD surface. The LCA60 epitope is shown in yellow, the MERS S4 epitope is shown in green, the overlapping C2/MCA1/m336 epitopes are shown in red and the overlapping JC57-14/D12/4C2/MERS-27 epitopes are shown in purple. **B**) The structure of SARS VHH-72 bound to the SARS-CoV-1 RBD is shown with SARS VHH-72 as dark blue ribbons and the SARS-CoV-1 RBD as a white molecular surface. Epitopes from previously reported crystal structures of the SARS-CoV-1 RBD bound by RBD-directed antibodies are shown as colored patches on the SARS-CoV-1 RBD surface. The 80R epitope is shown in blue, the S230 epitope is shown in yellow, the CR3022 epitope is shown in purple and the overlapping m396/F26G19 epitopes are shown in red. **C**) The SARS RBD is shown as a white molecular surface, ACE2 is shown as a transparent red molecular surface, SARS VHH-72 is shown as dark blue ribbons and CR3022 Fab is shown as purple ribbons.

STAR METHODS

RESOURCE AVAILABILITY

Lead Contact

Further information and requests for resources and reagents should be directed to and will be fulfilled by the Lead Contact, Jason S. McLellan (jmclellan@austin.utexas.edu).

Materials Availability

Plasmids generated in this study will be made available on request by the Lead Contact with a completed Materials Transfer Agreement (MTA).

Data and Code Availability

The X-ray crystallographic data and atomic models have been deposited at the Protein Data Bank with accession codes PDB: 6WAQ (SARS-CoV-1 RBD bound by SARS VHH-72) and PDB: 6WAR (MERS-CoV RBD bound by MERS VHH-55). The sequences of MERS VHH-55 and SARS VHH-72 have been deposited on GenBank under accession numbers MT350283 and MT350284. A list of software used in this study can be found in the Key Resources Table.

EXPERIMENTAL MODEL AND SUBJECT DETAILS

Cell Lines

FreeStyle293F cells (ThermoFisher Scientific) and HEK293-S cells (ThermoFisher Scientific) were cultured in FreeStyle293 expression media (Life Technologies), cultured at 37 °C with 8% CO_2 while shaking at 130 rpm. HEK293-T cells (ATCC) and Vero E6 cells (ATCC) were cultured at 37 °C in the presence of 5% CO_2 in DMEM supplemented with 10% heat-inactivated FBS, 1% penicillin, 1% streptomycin, 2 mM l-glutamine, non-essential amino acids (Invitrogen) and 1 mM sodium pyruvate. Huh7.5 cells (provided by Dr. Deborah R. Taylor) were cultured at 37 °C with 8% CO_2 in flasks with DMEM + 10% FBS. ExpiCHO-S cells (Gibco) were cultured at 37 °C with 8% CO_2 while shaking at 130 rpm in ExpiCHO expression media (Gibco). Cells lines were not tested for mycoplasma contamination nor authenticated.

METHOD DETAILS

Llama immunization

Llama immunizations and subsequent VHH library generation were performed by VIB Nanobody Core as follows. A llama, negative for antibodies against MERS-CoV and SARS-CoV-1 S glycoprotein, was subcutaneously immunized with approximately 150 µg recombinant SARS-CoV-1 S-2P protein on days 0, 7, 28 and 150 µg recombinant MERS-CoV S-2P protein on days 14 and 21 and 150 µg of both MERS-CoV S-2P and SARS-CoV-1 S-2P protein on day 35 (Kirchdoerfer et al., 2018; Pallesen et al., 2017). The adjuvant used was Gerbu LQ#3000. Immunizations and handling of the llama were performed according to directive 2010/63/EU of the European parliament for the protection of animals used for scientific purposes and approved by the Ethical Committee for Animal Experiments of the Vrije Universiteit Brussel (permit No. 13-601-1). Blood was collected 5 days after the last immunization for the preparation of lymphocytes. Total RNA from the peripheral blood lymphocytes was extracted and used as template for the first strand cDNA synthesis with oligo dT primer. Using this cDNA, the VHH encoding sequences were amplified by PCR and cloned between the *PstI* and *NotI* sites of the phagemid vector pMECS. In the pMECS vector, the VHH encoding sequence is followed by a linker, HA and His_6 tag (AAAYPYDVPDYGSHHHHHH). Electro-competent E.coli TG1 cells were transformed with the recombinant pMECS vector resulting in a VHH library of about 3×10^8 independent transformants. The resulting TG1 library stock was then infected with VCS M13 helper phages to obtain a library of VHH-presenting phages.

Isolation of MERS- and SARS-CoV VHH phages

Phages displaying MERS-CoV-specific VHHs were enriched after 2 rounds of biopanning on 20 µg of immobilized MERS-CoV S-2P protein in one well of a microtiter plate (type II, F96

Maxisorp, Nuc). For each panning round an uncoated well was used as a negative control. The wells were then washed 5 times with phosphate-buffered saline (PBS) + 0.05% Tween 20 and blocked with SEA BLOCK blocking buffer (Thermo Scientific) in the first panning round and 5% milk powder in PBS in the second panning round. About 10^{11} phages were added to the coated well and incubated for 1 hour at room temperature. Non-specifically bound phages were removed by washing with PBS + 0.05% Tween 20 (10 times in the first panning round and 15 times in the second panning round). The retained phages were eluted with TEA-solution (14% trimethylamine (Sigma) pH 10) and subsequently neutralized with 1 M Tris-HCl pH 8. The collected phages were amplified in exponentially growing *E.coli* TG1 cells, infected with VCS M13 helper phages and subsequently purified using PEG 8,000/NaCl precipitation for the next round of selection. Enrichment after each panning round was determined by infecting TG1 cells with 10-fold serial dilutions of the collected phages after which the bacteria were plated on LB agar plates with 100 μg mL^{-1} ampicillin and 1% glucose.

Phages displaying SARS-CoV-1 directed VHHs were enriched after 2 rounds of biopanning on 20 μg of SARS-CoV-1 S-2P protein captured with an anti-foldon antibody (generously provided by Dr. Vicente Mas) in one well of a microtiter plate (type II, F96 Maxisorp, Nuc). Before panning phages were first added to DS-Cav1 protein (McLellan et al., 2013) containing a C-terminal foldon domain, to deplete foldon specific phages. The unbound phages were next added to the coated well. Panning was performed as described above.

Periplasmic ELISA to select MERS- and SARS-CoV VHHs

After panning, 45 individual colonies of phage infected bacteria isolated after the first panning round on MERS-CoV S-2P or SARS-CoV-1 S-2P protein and 45 individual colonies isolated after

549 the second panning round on MERS-CoV S-2P or SARS-CoV-1 S-2P protein were randomly
550 selected for further analysis by ELISA for the presence of MERS-CoV and SARS-CoV-1 specific
551 VHHs, respectively. The individual colonies were inoculated in 2 mL of terrific broth (TB)
552 medium with 100 µg/mL ampicillin in 24-well deep well plates. After growing individual colonies
553 for 5 hours at 37 °C, isopropyl β-D-1-thiogalactopyranoside (IPTG) (1 mM) was added to induce
554 VHH expression during overnight incubation at 37 °C. To prepare periplasmic extract, the bacterial
555 cells were pelleted and resuspended in 250 µL TES buffer (0.2 M Tris-HCl pH 8, 0.5 mM EDTA,
556 0.5 M sucrose) and incubated at 4 °C for 30 min. Subsequently 350 µL water was added to induce
557 an osmotic shock. After 1-hour incubation at 4 °C followed by centrifugation, the periplasmic
558 extract was collected.
559 VHH-containing periplasmic extracts were then tested for binding to either MERS-CoV S-
560 2P or SARS-CoV-1 S-2P protein. Briefly, in the PE-ELISA screen after panning on MERS-CoV
561 S-2P protein, wells of microtiter plates (type II, F96 Maxisorp, Nuc) were coated overnight at 37
562 °C with 100 ng MERS-CoV S-2P (without foldon), MERS-CoV S-2P protein (with foldon) or as
563 negative controls coated with SARS-CoV-1 S-2P protein (with foldon), HCoV-HKU1 S-2P
564 (without foldon), DS-Cav1 (with foldon) or bovine serum albumin (BSA, Sigma-Aldrich). In the
565 PE-ELISA screen after panning on SARS-CoV-1 S protein wells of microtiter plates (type II, F96
566 Maxisorp, Nuc) were coated with 100 ng SARS-CoV-1 S-2P protein (with foldon), SARS-CoV-1
567 S-2P protein captured with an anti-foldon antibody (with foldon) or as negative controls coated
568 with MERS-CoV S-2P (without foldon), HCoV-HKU1 S-2P (without foldon), DS-Cav1 (with
569 foldon) or bovine serum albumin (BSA, Sigma-Aldrich). The coated plates were blocked with 5%
570 milk powder in PBS and 50 µL of the periplasmic extract was added to the wells. Bound VHHs
571 were detected with anti-HA (1/2,000, MMS-101P Biolegend) mAb followed by horseradish

peroxidase (HRP)-linked anti-mouse IgG (1/2,000, NXA931, GE Healthcare). Periplasmic fractions, for which the OD_{450} value of the antigen coated wells were at least two times higher than the OD_{450} value of the BSA coated wells, were considered to be specific for the coated antigen and selected for sequencing. The selected clones were grown in 3 mL of LB medium with 100 µg/mL ampicillin. The DNA of the selected colonies was isolated using the QIAprep Spin Miniprep kit (Qiagen) and sequenced using the MP057 primer (5'-TTATGCTTCCGGCTCGTATG-3').

VHH cloning into a *Pichia pastoris* expression vector

In order to express the MERS- and SARS-CoV VHHs in *Pichia pastoris*, the VHH encoding sequences were cloned in the pKai61 expression vector (described by Schoonooghe *et al.,* 2009) (Schoonooghe et al., 2009). In the vector, the VHH sequences contain a C-terminal 6x His-tag, are under the control of the methanol inducible AOX1 promotor and in frame with a modified version of the *S.cerevisae* α-mating factor prepro signal sequence. The vector contains a Zeocine resistance marker for selection in bacteria as well as in yeast cells. The VHH encoding sequences were amplified by PCR using the following forward and reverse primer (5'-GGCGGGTATCTCTCGAGAAAAGGCAGGTGCAGCTGCAGGAGTCTGGG-3') and (5'-CTAACTAGTCTAGTGATGGTGATGGTGGTGGCTGGAGACGGTGACCTGG-3') and cloned between the *Xho*I and *Spe*I sites in the pKai61 vector. The vectors were linearized by *PmeI* and transformed in the *Pichia pastoris* strain GS115 by electroporation at 1500 V using a Gene Pulser electroporator (Bio-Rad) *(Lin-Cereghino et al., 2005).* After transformation, the yeast cells were plated on YPD plates (1% (w/v) yeast extract, 2% (w/v) peptone, 2% (w/v) dextrose and 2% (w/v) agar) supplemented with zeocin (100 µg/mL) for selection.

Generating bivalent VHHs for *P. pastoris* expression

To generate bivalent tandem tail-to-head VHH constructs, the VHH sequence was amplified by PCR using the following forward (5'-GGGGTATCTCTCGAGAAAAGGCAGGTGCAGCTGGTGGAGTCTGGG-3') and reverse (5'-AGACTCCTGCAGCTGCACCTGACTACCGCCGCCTCCAGATCCACCTCCGCCACTACC GCCTCCGCCGCTGGAGACGGTGACCTGGG-3') primers, thereby removing a *Pst*I site from the beginning of the VHH coding sequence and adding a $(GGGGS)_3$ linker and the start of the VHH coding sequence with a *Pst*I site at the end of the sequence. After PCR, the fragment was cloned between the *XhoI* and *SpeI* sites in a SARS VHH-72 containing pKai61 vector, thereby generating a homo-bivalent construct. The vector containing this bivalent VHH was linearized and transformed in GS155 *Pichia pastoris* cells as outlined above.

Purification of MERS- and SARS-CoV VHHs from *Pichia*

The transformed *Pichia pastoris* clones were first expressed in 2 mL cultures. On day 1, 4 clones of each construct were inoculated in 2 mL of YPNG medium (2% pepton, 1% Bacto yeast extract, 1.34% YNB, 0.1 M potassium phosphate pH 6, 0.00004% biotin, 1% glycerol) with 100 µg/mL Zeocin (Life Technologies) and incubated while shaking at 28 °C for 24 hours. The next day, the cells were pelleted by centrifugation and the medium was replaced by YPNM medium (2% pepton, 1% Bacto yeast extract, 1.34% YNB, 0.1 M potassium phosphate pH 6.0, 1% methanol) to induce VHH expression. Cultures were incubated at 28 °C and 50 µL of 50% methanol was added at 16, 24 and 40 h. After 48 h, the yeast cells were pelleted and the supernatant was collected. The presence of soluble VHHs in the supernatants was verified using SDS-PAGE and subsequent

Coomassie Blue staining. VHH-containing supernatants of the different clones for each construct were pooled and the VHHs were purified using HisPur™ Ni-NTA Spin Plates (88230, Thermo Scientific™). Next, purified VHHs were concentrated on AcroPrep™ Advance 96-well filter plates for ultrafiltration 3 kDa cutoff (8033,Pall) and the imidazole-containing elution buffer was exchanged with PBS.

Production was scaled up (50 mL) for the VHHs with neutralizing capacity. Growth and methanol induction conditions and harvesting of medium were similar as mentioned above for the 2 mL cultures. The secreted VHHs in the medium were precipitated by ammonium sulfate $(NH_4)_2SO_4$ precipitation (80% saturation) for 4 h at 4 °C. The insoluble fraction was pelleted by centrifugation at 20,000 g and resuspended in 10 mL binding buffer (20 mM NaH_2PO_4 pH 7.5, 0.5M NaCl and 20 mM imidazole pH 7.4). The VHHs were purified from the solution using a 1 mL HisTrap HP column (GE Healthcare). To elute the bound VHHs a linear imidazole gradient starting from 20 mM and ending at 500 mM imidazole in binding buffer over a total volume of 20 mL was used. VHH containing fractions were pooled and concentrated and the elution buffer was exchanged with PBS with a Vivaspin column (5 kDa cutoff, GE Healthcare).

Enzyme-linked immunosorbent assay

Wells of microtiter plates (type II, F96 Maxisorp, Nuc) were coated overnight at 4 °C, respectively, with 100 ng recombinant MERS-CoV S-2P protein (with foldon), SARS-CoV-1 S-2P protein (with foldon), MERS-CoV RBD, MERS-CoV NTD, MERS-CoV S1, SARS-CoV-1 RBD, SARS-CoV-1 NTD or Fc-tagged SARS-CoV-2 RBD-SD1. The coated plates were blocked with 5% milk powder in PBS. Dilution series of the VHHs were added to the wells. Binding was detected by incubating the plates sequentially with either mouse anti-Histidine Tag antibody (MCA1396, Abd

Serotec) followed horseradish peroxidase (HRP)-linked anti-mouse IgG (1/2000, NXA931, GE Healthcare) or Streptavidin-HRP (554066, BD Biosciences) or by an HRP-linked rabbit anti-camelid VHH monoclonal antibody (A01861-200, GenScript). After washing 50 µL of TMB substrate (Tetramethylbenzidine, BD OptETA) was added to the plates and the reaction was stopped by addition of 50 µL of 1 M H_2SO4. The absorbance at 450 nM was measured with an iMark Microplate Absorbance Reader (Bio Rad). Curve fitting was performed using nonlinear regression (Graphpad 7.0).

CoV pseudovirus neutralization

Pseudovirus neutralization assay methods have been previously described (Pallesen et al., 2017; Wang et al., 2015). Briefly, pseudoviruses expressing spike genes for MERS-CoV England1 (GenBank ID: AFY13307) and SARS-CoV-1 Urbani (GenBank ID: AAP13441.1) were produced by co-transfection of plasmids encoding a luciferase reporter, lentivirus backbone, and spike genes in 293T cells (Wang et al., 2015). Serial dilutions of VHHs were mixed with pseudoviruses, incubated for 30 min at room temperature, and then added to previously-plated Huh7.5 cells. 72 hours later, cells were lysed, and relative luciferase activity was measured. Percent neutralization was calculated considering uninfected cells as 100% neutralization and cells transduced with only pseudovirus as 0% neutralization. IC_{50} titers were determined based on sigmoidal nonlinear regression.

To generate replication-deficient VSV pseudotyped viruses, HEK293T cells, transfected with MERS-CoV S, SARS-CoV-1 S or SARS-CoV-2 S were inoculated with a replication deficient VSV vector containing eGFP and firefly luciferase expression cassettes. After a 1 hour incubation at 37 °C, inoculum was removed, cells were washed with PBS and incubated in media

supplemented with an anti-VSV G mAb (ATCC) for 16 hours. Pseudotyped particles were then harvested and clarified by centrifugation (Berger Rentsch and Zimmer, 2011; Hoffmann, 2020). For the VSV pseudotype neutralization experiments, the pseudoviruses were incubated for 30 min at 37 °C with different dilutions of purified VHHs or with dilution series of culture supernatant of 293S cells that had been transfected with plasmids coding for SARS VHH-72 fused to human IgG1 Fc (VHH-72-Fc) or with GFP-binding protein (GBP: a VHH specific for GFP). The incubated pseudoviruses were subsequently added to confluent monolayers of Vero E6 cells. Sixteen hours later, the transduction efficiency was quantified by measuring the firefly luciferase activity in cell lysates using the firefly luciferase substrate of the dual-luciferase reporter assay system (Promega) and a Glowmax plate luminometer (Promega).

Mammalian protein expression and purification

Mammalian expression plasmids encoding SARS VHH72, MERS VHH55, residues 367-589 of MERS-CoV S (England1 strain), residues 320-502 of SARS-CoV-1 S (Tor2 strain), residues 307-510 of WIV1-CoV S, residues 319-591 of SARS-CoV-2 S, residues 1-281 of SARS-CoV-1 S (Tor2 strain), residues 1-351 of MERS-CoV S (England1 strain), residues 1-751 of MERS-CoV S (England1 strain), residues 1-1190 of SARS-CoV-1 S (Tor2 strain) with K968P and V969P substitutions (SARS-CoV-1 S-2P), residues 1-1291 of MERS-CoV S (England1 strain) with V1060P and L1061P substitutions (MERS S-2P), residues 1-1208 of SARS-CoV-2 S with K986P and V987P substitutions (SARS-CoV-2 S-2P), residues 1-615 of ACE2 and residues 40-766 of DPP4 were transfected into FreeStyle293 cells using polyethylenimine (PEI). All of these plasmids contained N-terminal signal sequences to ensure secretion into the cell supernatant. Supernatants were harvested and constructs containing C-terminal HRV3C cleavage sites, 8x

His-Tags and Twin-Strep-Tags (SARS VHH72, MERS VHH55, MERS-CoV S1, SARS-CoV-1 S-2P, MERS-CoV S-2P, SARS-CoV-2 S-2P, ACE2 and DPP4) were purified using Strep-Tactin resin (IBA). Constructs containing C-terminal HRV3C cleavage sites and Fc-tags (SARS-CoV-1 RBD, MERS-CoV RBD, WIV1-CoV RBD, SARS-CoV-2 RBD-SD1, SARS-CoV-1 NTD, MERS-CoV NTD) were purified using Protein A resin (Pierce). The SARS-CoV-1 RBD, MERS-CoV RBD, WIV1-CoV RBD, SARS-CoV-2 RBD-SD1, SARS VHH-72, MERS VHH-55, MERS-CoV NTD and SARS-CoV-1 NTD were then further purified using a Superdex 75 column (GE Healthcare) in 2 mM Tris pH 8.0, 200 mM NaCl and 0.02% NaN_3. MERS-CoV S1, SARS-CoV-1 S-2P, MERS-CoV S-2P, ACE2 and DPP4 were further purified using a Superose 6 column (GE Healthcare) in 2 mM Tris pH 8.0, 200 mM NaCl and 0.02% NaN_3.

HEK 293S cells were transfected with VHH-72-Fc or VHH-72-Fc (S) encoding plasmids using PEI. Briefly, suspension-adapted and serum-free HEK 293S cells were seeded at 3 x 10^6 cells/mL in Freestyle-293 medium (ThermoFisher Scientific). Next, 4.5 µg of pcDNA3.3-VHH72-Fc plasmid DNA was added to the cells and incubated on a shaking platform at 37 °C and 8% CO_2, for 5 min. Next, 9 µg of PEI was added to the cultures, and cells were further incubated for 5 h, after which an equal culture volume of Ex-Cell-293 (Sigma) was added to the cells. Transfections were incubated for 4 days, after which cells were pelleted (10', 300g) and supernatants were filtered before further use.

VHH-72-Fc was expressed in ExpiCHO cells (ThermoFisher Scientific), according to the manufacturer's protocol. Briefly, a 25 mL culture of 6 x10^6 cells/mL, grown at 37 °C and 8% CO_2 was transfected with 20 µg of pcDNA3.3-VHH-72-Fc plasmid DNA using ExpiFectamine CHO reagent. One day after transfection, 150 µL of ExpiCHO enhancer and 4 mL of ExpiCHO feed was added to the cells, and cultures were further incubated at 32 °C and 5% CO_2. Cells were

fed a second time 5 days post-transfection. Cultures were harvested as soon as cell viability dropped below 75%. For purification of the VHH-72-Fc, supernatants were loaded on a 5 mL MabSelect SuRe column (GE Healthcare). Unbound proteins were washed away with McIlvaine buffer pH 7.2, and bound proteins were eluted using McIlvaine buffer pH 3. Immediately after elution, protein-containing fractions were neutralized using a saturated Na_3PO_4 buffer. These neutralized fractions were then pooled, and loaded onto a HiPrep Desalting column for buffer exchange into storage buffer (25 mM L-Histidine, 125 mM NaCl).

Surface plasmon resonance

His-tagged SARS VHH-72 or MERS VHH-55 was immobilized to a single flow cell of an NTA sensorchip at a level of ~400 response units (RUs) per cycle using a Biacore X100 (GE Healthcare). The chip was doubly regenerated using 0.35 M EDTA and 0.1 M NaOH followed by 0.5 mM $NiCl_2$. Three samples containing only running buffer, composed of 10 mM HEPES pH 8.0, 150 mM NaCl and 0.005% Tween 20, were injected over both ligand and reference flow cells, followed by either SARS-CoV-1 RBD, WIV1-CoV RBD, SARS-CoV-2 RBD-SD1 or MERS-CoV RBD serially diluted from 50-1.56 nM, with a replicate of the 3.1 nM concentration. The resulting data were double-reference subtracted and fit to a 1:1 binding model using the Biacore X100 Evaluation software.

Crystallization and data collection

Plasmids encoding for MERS VHH-55 and residues 367-589 of MERS-CoV S with a C-terminal HRV3C cleavage site and a monomeric human Fc tag were co-transfected into kifunensin-treated FreeStyle 293F cells, as described above. After purifying the cell supernatant with Protein A

resin, the immobilized complex was treated with HRV3C protease and Endoglycosidase H to remove both tags and glycans. The complex was then purified using a Superdex 75 column in 2 mM Tris pH 8.0, 200 mM NaCl and 0.02% NaN_3. The purified complex was then concentrated to 5.0 mg/mL and used to prepare hanging-drop crystallization trays. Crystals grown in 1.0 M Na/K phosphate pH 7.5 were soaked in mother liquor supplemented with 20% ethylene glycol and frozen in liquid nitrogen. Diffraction data were collected to a resolution of 3.40 Å at the SBC beamline 19-ID (APS, Argonne National Laboratory)

Plasmids encoding for SARS VHH-72 and residues 320-502 of SARS-CoV-1 S with a C-terminal HRV3C cleavage site and a monomeric human Fc tag were co-transfected into kifunensin-treated FreeStyle 293F cells, as described above. After purifying the cell supernatant with Protein A resin, the immobilized complex was treated with HRV3C protease and Endoglycosidase H to remove both tags and glycans. The processed complex was subjected to size-exclusion chromatography using a Superdex 75 column in 2 mM Tris pH 8.0, 200 mM NaCl and 0.02% NaN_3. The purified complex was then concentrated to 10.0 mg/mL and used to prepare hanging-drop crystallization trays. Crystals grown in 0.1 M Tris pH 8.5, 0.2 M $LiSO_4$, 0.1 M LiCl and 8% PEG 8000 were soaked in mother liquor supplemented with 20% glycerol and frozen in liquid nitrogen. Diffraction data were collected to a resolution of 2.20 Å at the SBC beamline 19-ID (APS, Argonne National Laboratory)

Structure determination

Diffraction data for both complexes were indexed and integrated using iMOSFLM before being scaled in AIMLESS (Battye et al., 2011; Evans and Murshudov, 2013). The SARS-CoV-1 RBD+SARS VHH-72 dataset was phased by molecular replacement in PhaserMR using

coordinates from PDBs 2AJF and 5F1O as search ensembles (McCoy, 2007). The MERS-CoV RBD+MERS VHH-55 dataset was also phased by molecular replacement in PhaserMR using coordinates from PDBs 4L72 and 5F1O as search ensembles. The resulting molecular replacement solutions were iteratively rebuilt and refined using Coot, ISOLDE and Phenix (Adams et al., 2002; Croll, 2018; Emsley and Cowtan, 2004). The MERS-CoV+MERS VHH-55 structure was refined using NCS. Crystallographic software packages were curated by SBGrid (Morin et al., 2013).

Biolayer interferometry

Anti-human capture (AHC) tips (FortéBio) were soaked in running buffer composed of 10 mM HEPES pH 7.5, 150 mM NaCl, 3 mM EDTA, 0.005% Tween 20 and 1 mg/mL BSA for 20 min before being used to capture either Fc-tagged SARS-CoV-1 RBD, Fc-tagged SARS-CoV-2 RBD-SD1 or Fc-tagged MERS-CoV RBD to a level of 0.8 nm in an Octet RED96 (FortéBio). Tips were then dipped into either 100 nM MERS VHH-55 or 100 nM SARS VHH-72. Tips were next dipped into wells containing either 1 μM ACE2 or 100 nM DPP4 supplemented with the nanobody that the tip had already been dipped into to ensure continued saturation. Data were reference-subtracted and aligned to each other in Octet Data Analysis software v11.1 (FortéBio) based on a baseline measurement that was taken before being dipped into the final set of wells that contained either ACE2 or DPP4.

BLI measurements were also performed with VHH-72-Fc fusion produced in HEK 293S cells. SARS-CoV-2 RBD with a mouse IgG1 Fc tag (Sino Biological) was immobilized to an anti-mouse IgG Fc capture (AMC) tip (FortéBio) to a response level of 0.5 nm. Supernatant of non-transfected and VHH-72-Fc transfected HEK293-S cells was applied in a three-fold dilution

series in kinetics buffer. Binding was measured at 30 °C, with baseline and dissociation measured in equal dilution of non-transformed HEK293S supernatant in kinetics buffer. Between analyses, biosensors were regenerated by three times 20 s exposure to regeneration buffer (10 mM glycine pH 1.7).

Flow cytometry

Binding of VHH-72-Fc, VHH-72-Fc (S) and monomeric and bivalent SARS VHH-72 to SARS-CoV-1 and SARS-CoV-2 S was analyzed by flow cytometry using cells transfected with a GFP expression plasmid combined with an expression plasmid for either SARS-CoV-1 or SARS-Cov-2 S. HEK 293S culture media (1/20 diluted in PBS + 0.5%BSA) of VHH-72-Fc and VHH-72-Fc (S) transformants were incubated with transfected cells. Binding of the VHH-72-Fc and VHH-72-Fc (S) to cells was detected with an AF633 conjugated goat anti-human IgG antibody, whereas binding of monomeric and bivalent VHHs to SARS-CoV-1 or SARS-CoV-2 S was detected with a mouse anti-HisTag antibody and an AF647 conjugated donkey anti-mouse IgG antibody. Binding was calculated as the mean AF633 fluorescence intensity (MFI) of GFP expressing cells (GFP^+) divided by the MFI of GFP negative cells (GFP^-).

RBD competition assay on Vero E6 cells

SARS-CoV-2 RBD fused to murine IgG Fc (Sino Biological) at a final concentration of 0.4 μg/mL was incubated with a dilution series of tail-to-head bivalent VHHs or VHH-Fc fusions and incubated at room temperature for 20 min before an additional 10 min incubation on ice. Vero E6 cells grown at sub-confluency were detached by cell dissociation buffer (Sigma) and trypsin treatment. After washing once with PBS the cells were blocked with 1% BSA in PBS on ice. All remaining steps were also performed on ice. The mixtures containing RBD and tail-to-

head bivalent VHHs or VHH-Fc fusions were added to the cells and incubated for one hour. Subsequently, the cells were washed 3 times with PBS containing 0.5% BSA and stained with an AF647 conjugated donkey anti-mouse IgG antibody (Invitrogen) for 1 hour. Following additional 3 washes with PBS containing 0.5% BSA, the cells were analyzed by flow cytometry using an BD LSRII flow cytometer (BD Biosciences).

QUANTIFICATION AND STATISTICAL ANALYSIS

Binding and neutralization assays were conducted with at least duplicate measurements and presented as the mean ± SEM of the indicated number of replicates. Details can be found in figure legends.

ACKNOWLEDGEMENTS

We thank members of the McLellan Laboratory for providing helpful comments on the manuscript. We would like to thank Dr. John Ludes-Meyers for assistance with cell transfection and protein production. This work was supported by a National Institutes of Health (NIH)/National Institute of Allergy and Infectious Disease (NIAID) grant R01-AI127521 (to J.S.M.), and in part by intramural NIAID funding. Research was supported by funding from VIB, Ghent University GOA project to N.C. and X.S., FWO and VLAIO fellowships and research projects to various VIB-CMB COVID-19 response team members. We acknowledge the team of the VIB Nanobody Service Facility for their services. D.D.V. was supported by a FWOsb fellowship, W.V. by the FWO -SBO grant “GlycoDelete”, S.P. by BMBF (RAPID consortium, 01K11723D), and B.S. by FWO-EOS project VIREOS. We are deeply indebted to the VIB-CMB COVID-19 response team members, who volunteered to offer their expertise and agile work under conditions of almost complete lockdown and societal standstill. We thank the

support staff of both VIB-IRC and VIB-CMB centers, the members of VIB Discovery Sciences units' COVID-19 team for rapid and consistent support and input. Argonne is operated by UChicago Argonne, LLC, for the US Department of Energy (DOE), Office of Biological and Environmental Research under Contract DE-AC02-06CH11357.

AUTHOR CONTRIBUTIONS

Conceptualization, D.W., D.D.V., B.S.G., B.S., N.C., X.S., and J.S.M.; Investigation and visualization, D.W., D.D.V., K.S.C., G.M.T., N.W., W.V.B., K.R., L.v.S., M.H., S.P., and B.S.; Writing - Original Draft, D.W. and D.D.V.; Writing – Reviewing & Editing, D.W., D.D.V., K.S.C., G.M.T., N.W., B.S.G., N.C., B.S., X.S., and J.S.M.; Supervision, B.S.G., N.C., B.S., X.S., and J.S.M.

DECLARATIONS OF INTEREST

K.S.C., N.W., B.S.G. and J.S.M. are inventors on US patent application no. 62/412,703, entitled "Prefusion Coronavirus Spike Proteins and Their Use". D.W., K.S.C., N.W., B.S.G., and J.S.M. are inventors on US patent application no. 62/972,886, entitled "2019-nCoV Vaccine." D.W., D.D.V., B.S.G., B.S., X.S., and J.S.M. are inventors on US patent application no. 62/988,610, entitled "Coronavirus Binders". D.W., N.C., B.S., X.S., and J.S.M. are inventors on US patent application no. 62/991,408, entitled "SARS-CoV-2 Virus Binders".

REFERENCES

Adams, P.D., Grosse-Kunstleve, R.W., Hung, L.W., Ioerger, T.R., McCoy, A.J., Moriarty, N.W., Read, R.J., Sacchettini, J.C., Sauter, N.K., and Terwilliger, T.C. (2002). PHENIX: building new software for automated crystallographic structure determination. Acta Crystallogr D Biol Crystallogr *58*, 1948-1954.

Battye, T.G., Kontogiannis, L., Johnson, O., Powell, H.R., and Leslie, A.G. (2011). iMOSFLM: a new graphical interface for diffraction-image processing with MOSFLM. Acta Crystallogr D Biol Crystallogr *67*, 271-281.

Berger Rentsch, M., and Zimmer, G. (2011). A vesicular stomatitis virus replicon-based bioassay for the rapid and sensitive determination of multi-species type I interferon. PLoS One *6*, e25858.

Bosch, B.J., van der Zee, R., de Haan, C.A., and Rottier, P.J. (2003). The coronavirus spike protein is a class I virus fusion protein: structural and functional characterization of the fusion core complex. J Virol *77*, 8801-8811.

Chan, J.F., Yuan, S., Kok, K.H., To, K.K., Chu, H., Yang, J., Xing, F., Liu, J., Yip, C.C., Poon, R.W.*, et al.* (2020). A familial cluster of pneumonia associated with the 2019 novel coronavirus indicating person-to-person transmission: a study of a family cluster. Lancet *395*, 514-523.

Chen, Z., Bao, L., Chen, C., Zou, T., Xue, Y., Li, F., Lv, Q., Gu, S., Gao, X., Cui, S.*, et al.* (2017). Human Neutralizing Monoclonal Antibody Inhibition of Middle East Respiratory Syndrome Coronavirus Replication in the Common Marmoset. J Infect Dis *215*, 1807-1815.

Croll, T.I. (2018). ISOLDE: a physically realistic environment for model building into low-resolution electron-density maps. Acta Crystallogr D Struct Biol *74*, 519-530.

De Vlieger, D., Ballegeer, M., Rossey, I., Schepens, B., and Saelens, X. (2018). Single-Domain Antibodies and Their Formatting to Combat Viral Infections. Antibodies (Basel) *8*.

Detalle, L., Stohr, T., Palomo, C., Piedra, P.A., Gilbert, B.E., Mas, V., Millar, A., Power, U.F., Stortelers, C., Allosery, K.*, et al.* (2016). Generation and Characterization of ALX-0171, a Potent Novel Therapeutic Nanobody for the Treatment of Respiratory Syncytial Virus Infection. Antimicrob Agents Chemother *60*, 6-13.

Dumoulin, M., Conrath, K., Van Meirhaeghe, A., Meersman, F., Heremans, K., Frenken, L.G., Muyldermans, S., Wyns, L., and Matagne, A. (2002). Single-domain antibody fragments with high conformational stability. Protein Sci *11*, 500-515.

Emsley, P., and Cowtan, K. (2004). Coot: model-building tools for molecular graphics. Acta Crystallogr D Biol Crystallogr *60*, 2126-2132.

Evans, P.R., and Murshudov, G.N. (2013). How good are my data and what is the resolution? Acta Crystallogr D Biol Crystallogr *69*, 1204-1214.

Forsman, A., Beirnaert, E., Aasa-Chapman, M.M., Hoorelbeke, B., Hijazi, K., Koh, W., Tack, V., Szynol, A., Kelly, C., McKnight, A.*, et al.* (2008). Llama antibody fragments with cross-subtype human immunodeficiency virus type 1 (HIV-1)-neutralizing properties and high affinity for HIV-1 gp120. J Virol *82*, 12069-12081.

Gaunt, E.R., Hardie, A., Claas, E.C., Simmonds, P., and Templeton, K.E. (2010). Epidemiology and clinical presentations of the four human coronaviruses 229E, HKU1, NL63, and OC43 detected over 3 years using a novel multiplex real-time PCR method. J Clin Microbiol *48*, 2940-2947.

Ge, X.Y., Li, J.L., Yang, X.L., Chmura, A.A., Zhu, G., Epstein, J.H., Mazet, J.K., Hu, B., Zhang, W., Peng, C.*, et al.* (2013). Isolation and characterization of a bat SARS-like coronavirus that uses the ACE2 receptor. Nature *503*, 535-538.

Govaert, J., Pellis, M., Deschacht, N., Vincke, C., Conrath, K., Muyldermans, S., and Saerens, D. (2012). Dual beneficial effect of interloop disulfide bond for single domain antibody fragments. J Biol Chem *287*, 1970-1979.

Gui, M., Song, W., Zhou, H., Xu, J., Chen, S., Xiang, Y., and Wang, X. (2017). Cryo-electron microscopy structures of the SARS-CoV spike glycoprotein reveal a prerequisite conformational state for receptor binding. Cell Res *27*, 119-129.

Hamers-Casterman, C., Atarhouch, T., Muyldermans, S., Robinson, G., Hamers, C., Songa, E.B., Bendahman, N., and Hamers, R. (1993). Naturally occurring antibodies devoid of light chains. Nature *363*, 446-448.

Hoffmann, M.K.-W., H; Krüger, N; Müller, M; Drosten, C; Pöhlmann, S. (2020). The novel coronavirus 2019 (2019-nCoV) uses the SARS-coronavirus receptor ACE2 and the cellular protease TMPRSS2 for entry into target cells. bioRxiv.

Huang, C., Wang, Y., Li, X., Ren, L., Zhao, J., Hu, Y., Zhang, L., Fan, G., Xu, J., Gu, X.*, et al.* (2020). Clinical features of patients infected with 2019 novel coronavirus in Wuhan, China. Lancet *395*, 497-506.

Hwang, W.C., Lin, Y., Santelli, E., Sui, J., Jaroszewski, L., Stec, B., Farzan, M., Marasco, W.A., and Liddington, R.C. (2006). Structural basis of neutralization by a human anti-severe acute respiratory syndrome spike protein antibody, 80R. J Biol Chem *281*, 34610-34616.

Ibanez, L.I., De Filette, M., Hultberg, A., Verrips, T., Temperton, N., Weiss, R.A., Vandevelde, W., Schepens, B., Vanlandschoot, P., and Saelens, X. (2011). Nanobodies with in vitro neutralizing activity protect mice against H5N1 influenza virus infection. J Infect Dis *203*, 1063-1072.

Kirchdoerfer, R.N., Cottrell, C.A., Wang, N., Pallesen, J., Yassine, H.M., Turner, H.L., Corbett, K.S., Graham, B.S., McLellan, J.S., and Ward, A.B. (2016). Pre-fusion structure of a human coronavirus spike protein. Nature *531*, 118-121.

Kirchdoerfer, R.N., Wang, N., Pallesen, J., Wrapp, D., Turner, H.L., Cottrell, C.A., Corbett, K.S., Graham, B.S., McLellan, J.S., and Ward, A.B. (2018). Stabilized coronavirus spikes are resistant to conformational changes induced by receptor recognition or proteolysis. Sci Rep *8*, 15701.

Koch, K., Kalusche, S., Torres, J.L., Stanfield, R.L., Danquah, W., Khazanehdari, K., von Briesen, H., Geertsma, E.R., Wilson, I.A., Wernery, U.*, et al.* (2017). Selection of nanobodies with broad neutralizing potential against primary HIV-1 strains using soluble subtype C gp140 envelope trimers. Sci Rep *7*, 8390.

Ksiazek, T.G., Erdman, D., Goldsmith, C.S., Zaki, S.R., Peret, T., Emery, S., Tong, S., Urbani, C., Comer, J.A., Lim, W.*, et al.* (2003). A novel coronavirus associated with severe acute respiratory syndrome. N Engl J Med *348*, 1953-1966.

Lan, J.G., J; Yu, J; Shan, S; Zhou, H; Fan, S; Zhang, Q; Shi, X; Wang, Q; Zhang, L; Wang, X. (2020). Crystal structure of the 2019-nCoV spike receptor-binding domain bound with the ACE2 receptor. bioRxiv.

Larios Mora, A., Detalle, L., Gallup, J.M., Van Geelen, A., Stohr, T., Duprez, L., and Ackermann, M.R. (2018). Delivery of ALX-0171 by inhalation greatly reduces respiratory syncytial virus disease in newborn lambs. MAbs *10*, 778-795.

Laursen, N.S., Friesen, R.H.E., Zhu, X., Jongeneelen, M., Blokland, S., Vermond, J., van Eijgen, A., Tang, C., van Diepen, H., Obmolova, G.*, et al.* (2018). Universal protection against influenza infection by a multidomain antibody to influenza hemagglutinin. Science *362*, 598-602.

Li, F., Li, W., Farzan, M., and Harrison, S.C. (2005). Structure of SARS coronavirus spike receptor-binding domain complexed with receptor. Science *309*, 1864-1868.

Li, W., Moore, M.J., Vasilieva, N., Sui, J., Wong, S.K., Berne, M.A., Somasundaran, M., Sullivan, J.L., Luzuriaga, K., Greenough, T.C.*, et al.* (2003). Angiotensin-converting enzyme 2 is a functional receptor for the SARS coronavirus. Nature *426*, 450-454.

Li, Y., Wan, Y., Liu, P., Zhao, J., Lu, G., Qi, J., Wang, Q., Lu, X., Wu, Y., Liu, W.*, et al.* (2015). A humanized neutralizing antibody against MERS-CoV targeting the receptor-binding domain of the spike protein. Cell Res *25*, 1237-1249.

Lin-Cereghino, J., Wong, W.W., Xiong, S., Giang, W., Luong, L.T., Vu, J., Johnson, S.D., and Lin-Cereghino, G.P. (2005). Condensed protocol for competent cell preparation and transformation of the methylotrophic yeast Pichia pastoris. Biotechniques *38*, 44, 46, 48.

Lu, R., Zhao, X., Li, J., Niu, P., Yang, B., Wu, H., Wang, W., Song, H., Huang, B., Zhu, N.*, et al.* (2020). Genomic characterisation and epidemiology of 2019 novel coronavirus: implications for virus origins and receptor binding. Lancet *395*, 565-574.

McCoy, A.J. (2007). Solving structures of protein complexes by molecular replacement with Phaser. Acta Crystallogr D Biol Crystallogr *63*, 32-41.

McLellan, J.S., Chen, M., Joyce, M.G., Sastry, M., Stewart-Jones, G.B., Yang, Y., Zhang, B., Chen, L., Srivatsan, S., Zheng, A.*, et al.* (2013). Structure-based design of a fusion glycoprotein vaccine for respiratory syncytial virus. Science *342*, 592-598.

Morin, A., Eisenbraun, B., Key, J., Sanschagrin, P.C., Timony, M.A., Ottaviano, M., and Sliz, P. (2013). Collaboration gets the most out of software. Elife *2*, e01456.

Pak, J.E., Sharon, C., Satkunarajah, M., Auperin, T.C., Cameron, C.M., Kelvin, D.J., Seetharaman, J., Cochrane, A., Plummer, F.A., Berry, J.D.*, et al.* (2009). Structural insights into immune recognition of the severe acute respiratory syndrome coronavirus S protein receptor binding domain. J Mol Biol *388*, 815-823.

Pallesen, J., Wang, N., Corbett, K.S., Wrapp, D., Kirchdoerfer, R.N., Turner, H.L., Cottrell, C.A., Becker, M.M., Wang, L., Shi, W.*, et al.* (2017). Immunogenicity and structures of a rationally designed prefusion MERS-CoV spike antigen. Proc Natl Acad Sci U S A *114*, E7348-E7357.

Prabakaran, P., Gan, J., Feng, Y., Zhu, Z., Choudhry, V., Xiao, X., Ji, X., and Dimitrov, D.S. (2006). Structure of severe acute respiratory syndrome coronavirus receptor-binding domain complexed with neutralizing antibody. J Biol Chem *281*, 15829-15836.

Raj, V.S., Mou, H., Smits, S.L., Dekkers, D.H., Muller, M.A., Dijkman, R., Muth, D., Demmers, J.A., Zaki, A., Fouchier, R.A.*, et al.* (2013). Dipeptidyl peptidase 4 is a functional receptor for the emerging human coronavirus-EMC. Nature *495*, 251-254.

Respaud, R., Vecellio, L., Diot, P., and Heuze-Vourc'h, N. (2015). Nebulization as a delivery method for mAbs in respiratory diseases. Expert Opin Drug Deliv *12*, 1027-1039.

Rossey, I., Gilman, M.S., Kabeche, S.C., Sedeyn, K., Wrapp, D., Kanekiyo, M., Chen, M., Mas, V., Spitaels, J., Melero, J.A.*, et al.* (2017). Potent single-domain antibodies that arrest respiratory syncytial virus fusion protein in its prefusion state. Nat Commun *8*, 14158.

Rotman, M., Welling, M.M., van den Boogaard, M.L., Moursel, L.G., van der Graaf, L.M., van Buchem, M.A., van der Maarel, S.M., and van der Weerd, L. (2015). Fusion of hIgG1-Fc to 111In-anti-amyloid single domain antibody fragment VHH-pa2H prolongs blood residential time in APP/PS1 mice but does not increase brain uptake. Nucl Med Biol *42*, 695-702.

Schoonooghe, S., Kaigorodov, V., Zawisza, M., Dumolyn, C., Haustraete, J., Grooten, J., and Mertens, N. (2009). Efficient production of human bivalent and trivalent anti-MUC1 Fab-scFv antibodies in Pichia pastoris. BMC Biotechnol *9*, 70.

Stalin Raj, V., Okba, N.M.A., Gutierrez-Alvarez, J., Drabek, D., van Dieren, B., Widagdo, W., Lamers, M.M., Widjaja, I., Fernandez-Delgado, R., Sola, I.*, et al.* (2018). Chimeric camel/human heavy-chain antibodies protect against MERS-CoV infection. Sci Adv *4*, eaas9667.

Tian, X., Li, C., Huang, A., Xia, S., Lu, S., Shi, Z., Lu, L., Jiang, S., Yang, Z., Wu, Y.*, et al.* (2020). Potent binding of 2019 novel coronavirus spike protein by a SARS coronavirus-specific human monoclonal antibody. Emerg Microbes Infect *9*, 382-385.

van der Linden, R.H., Frenken, L.G., de Geus, B., Harmsen, M.M., Ruuls, R.C., Stok, W., de Ron, L., Wilson, S., Davis, P., and Verrips, C.T. (1999). Comparison of physical chemical properties of llama VHH antibody fragments and mouse monoclonal antibodies. Biochim Biophys Acta *1431*, 37-46.

Walls, A.C., Tortorici, M.A., Bosch, B.J., Frenz, B., Rottier, P.J.M., DiMaio, F., Rey, F.A., and Veesler, D. (2016). Cryo-electron microscopy structure of a coronavirus spike glycoprotein trimer. Nature *531*, 114-117.

Walls, A.C., Xiong, X., Park, Y.J., Tortorici, M.A., Snijder, J., Quispe, J., Cameroni, E., Gopal, R., Dai, M., Lanzavecchia, A.*, et al.* (2019). Unexpected Receptor Functional Mimicry Elucidates Activation of Coronavirus Fusion. Cell *176*, 1026-1039 e1015.

Walls, A.P., Y-J; Tortorici, MA; Wall, A; McGuire, AT; Veesler, D. (2020). Structure, function and antigenicity of the SARS-CoV-2 spike glycoprotein. Cell.

Wan, Y., Shang, J., Graham, R., Baric, R.S., and Li, F. (2020). Receptor recognition by novel coronavirus from Wuhan: An analysis based on decade-long structural studies of SARS. J Virol.

Wang, L., Shi, W., Chappell, J.D., Joyce, M.G., Zhang, Y., Kanekiyo, M., Becker, M.M., van Doremalen, N., Fischer, R., Wang, N.*, et al.* (2018). Importance of Neutralizing Monoclonal Antibodies Targeting Multiple Antigenic Sites on the Middle East Respiratory Syndrome Coronavirus Spike Glycoprotein To Avoid Neutralization Escape. J Virol *92*.

Wang, L., Shi, W., Joyce, M.G., Modjarrad, K., Zhang, Y., Leung, K., Lees, C.R., Zhou, T., Yassine, H.M., Kanekiyo, M.*, et al.* (2015). Evaluation of candidate vaccine approaches for MERS-CoV. Nat Commun *6*, 7712.

Wang, N., Shi, X., Jiang, L., Zhang, S., Wang, D., Tong, P., Guo, D., Fu, L., Cui, Y., Liu, X.*, et al.* (2013). Structure of MERS-CoV spike receptor-binding domain complexed with human receptor DPP4. Cell Res *23*, 986-993.

Wang, Q., Qi, J., Yuan, Y., Xuan, Y., Han, P., Wan, Y., Ji, W., Li, Y., Wu, Y., Wang, J.*, et al.* (2014). Bat origins of MERS-CoV supported by bat coronavirus HKU4 usage of human receptor CD26. Cell Host Microbe *16*, 328-337.

Woo, P.C., Lau, S.K., Huang, Y., and Yuen, K.Y. (2009). Coronavirus diversity, phylogeny and interspecies jumping. Exp Biol Med (Maywood) *234*, 1117-1127.

Wrapp, D., and McLellan, J.S. (2019). The 3.1 A cryo-EM structure of the porcine epidemic diarrhea virus spike protein in the prefusion conformation. J Virol.

Wrapp, D., Wang, N., Corbett, K.S., Goldsmith, J.A., Hsieh, C.L., Abiona, O., Graham, B.S., and McLellan, J.S. (2020). Cryo-EM structure of the 2019-nCoV spike in the prefusion conformation. Science.

Yan, R.Z., Y; Li, Y; Xia, L; Guo, Y; Zhou, Q. (2020). Structural basis for the recognition of the SARS-CoV-2 by full-length human ACE2. Science.

Ying, T., Prabakaran, P., Du, L., Shi, W., Feng, Y., Wang, Y., Wang, L., Li, W., Jiang, S., Dimitrov, D.S*., et al.* (2015). Junctional and allele-specific residues are critical for MERS-CoV neutralization by an exceptionally potent germline-like antibody. Nat Commun *6*, 8223.

Yu, X., Zhang, S., Jiang, L., Cui, Y., Li, D., Wang, D., Wang, N., Fu, L., Shi, X., Li, Z*., et al.* (2015). Structural basis for the neutralization of MERS-CoV by a human monoclonal antibody MERS-27. Sci Rep *5*, 13133.

Yuan M, W.N., Zhu X, Lee C-CD, So RTY, Lv H, Mok CKP, Wilson IA. (2020). A highly conserved cryptic epitope in the receptor-binding domains of SARS-CoV-2 and SARS-CoV. bioRxiv.

Yuan, Y., Cao, D., Zhang, Y., Ma, J., Qi, J., Wang, Q., Lu, G., Wu, Y., Yan, J., Shi, Y*., et al.* (2017). Cryo-EM structures of MERS-CoV and SARS-CoV spike glycoproteins reveal the dynamic receptor binding domains. Nat Commun *8*, 15092.

Zaki, A.M., van Boheemen, S., Bestebroer, T.M., Osterhaus, A.D., and Fouchier, R.A. (2012). Isolation of a novel coronavirus from a man with pneumonia in Saudi Arabia. N Engl J Med *367*, 1814-1820.

Zhao, G., He, L., Sun, S., Qiu, H., Tai, W., Chen, J., Li, J., Chen, Y., Guo, Y., Wang, Y*., et al.* (2018). A Novel Nanobody Targeting Middle East Respiratory Syndrome Coronavirus (MERS-CoV) Receptor-Binding Domain Has Potent Cross-Neutralizing Activity and Protective Efficacy against MERS-CoV. J Virol *92*.

Zhou, P., Yang, X.L., Wang, X.G., Hu, B., Zhang, L., Zhang, W., Si, H.R., Zhu, Y., Li, B., Huang, C.L*., et al.* (2020). A pneumonia outbreak associated with a new coronavirus of probable bat origin. Nature.

KEY RESOURCES TABLE

REAGENT or RESOURCE	SOURCE	IDENTIFIER
Antibodies		
Anti-VSV-G antibody (I1, produced from CRL-2700 mouse hybridoma cells)	ATCC	Cat.# CRL-2700 RRID:CVCL_G654
Anti-foldon antibody	Provided by Dr. Vicente Mas Insituto de Salud Carlos III: National Centre for Microbiology	N/A
Purified anti-HA.11 Epitope Tag Antibody	Biolegend	Cat# MMS-101P
Mouse IgG HRP Linked Whole Ab	GE Healthcare	Cat# NXA931
Mouse anti Histidine Tag	Bio-Rad	Cat# MCA1396
Streptavidin-HRP	BD Biosciences	Cat#554066
Rabbit anti-camelid VHH HRP	GenScript	Cat# A01861-200
Alexa fluor 647 donkey anti mouse IgG	Invitrogen	Cat# A31571
Alexa fluor 633 goat anti human IgG	Invitrogen	Cat# A21091
Bacterial and Virus Strains		
TG1 cells	Immunosource	Cat# 60502-2
Gerbu LQ#3000	Gerbu Biotechnik	Cat# 3000-25
VSV*ΔG-FLuc	PMID: 21998709	N/A
SARS-CoV-1 S pseudotype VSV	PMID: 32142651	https://doi.org/10.1016/j.cell.2020.02.052
SARS-CoV-2 S pseudotype VSV	PMID: 32142651	https://doi.org/10.1016/j.cell.2020.02.052
Chemicals, Peptides, and Recombinant Proteins		
Trimethylamine (TEA) solution	Sigma-Aldrich	Cat# 471283
Zeocin	Gibco	Cat# R25001
MERS-CoV S-2P protein	PMID: 28807998	N/A
SARS-CoV-1 S-2P protein	PMID: 28807998	N/A
SARS VHH-72 protein	This manuscript	N/A
MERS VHH-55 protein	This manuscript	N/A
SARS-CoV-2 S-2P protein	PMID: 32075877	N/A
DS-Cav1 protein	PMID: 24179220	N/A
MERS-CoV RBD protein	PMID: 23835475	N/A
MERS-CoV NTD protein	PMID: 28807998	N/A
MERS-CoV S1 protein	This manuscript	N/A
SARS-CoV-1 RBD protein	PMID: 32075877	N/A
SARS-CoV-1 NTD protein	This manuscript	N/A
WIV1-CoV RBD protein	This manuscript	N/A
SARS-CoV-2 RBD-SD1 protein	PMID: 32075877	N/A
ACE2 protein	PMID: 30356097	N/A
DPP4 protein	PMID: 28807998	N/A
SARS-CoV-2 RBD Fc protein	Sino Biological	Cat# 40592-V05H
VHH-23 protein	PMID: 31921179	N/A
Bovine serum Albumin	Sigma-Aldrich	Cat# A8327
Anti-Mouse IgG Fc Capture (AMC) Biosensors	FortéBio	Cat# 18-5090

Polyethylenimine, Linear, MW 25000, Transfection Grade (PEI 25K)	Polysciences	Cat# 23966-1
ExpiCHO™ Expression Medium	Gibco	A2910001
FreeStyle™ 293 Expression Medium	Gibco	Cat# 12338002
EX-CELL® 293 Serum-Free Medium	Sigma-Aldrich	Cat# 14571C
Kifunensin	GlycoSyn	Cat# FC-034
25 kDa linear polyethylenimine	Polysciences	Cat# 3966-2
Critical Commercial Assays		
Dual-Luciferase® Reporter Assay System	Promega	Cat# E1910
TMB Substrate Reagent Set	BD Pharmingen	Cat# 555214
pcDNA™3.3-TOPO® TA Cloning Kit	Invitrogen	Cat# K8300-01
NEBNext® dA-Tailing Module	New England Biolabs	Cat# E6053
ExpiFectamine™ CHO Transfection Kit	Gibco	Cat# A29129
NucleoBond Xtra Midi kit	Macherey-Nagel	Cat# MN740410.100
FuGENE® HD Transfection Reagent	Promega	Cat# E2311
Deposited Data		
Crystal structure of SARS-CoV-1 RBD + SARS VHH-72	This manuscript	PDB ID: 6WAQ
Crystal structure of MERS-CoV RBD + MERS VHH-55	This manuscript	PDB ID: 6WAR
SARS VHH-72 sequence	This manuscript	GenBank ID: MT350284
MERS VHH-55 sequence	This manuscript	GenBank ID: MT350283
Experimental Models: Cell Lines		
Huh7.5 cells	Provided by Dr. Deborah R. Taylor of the US FDA	N/A
Freestyle 293F cells	ThermoFisher Scientific	Cat# R7007
Vero E6 cells	ATCC	Cat# CRL-1586
HEK293T cells	ATCC	Cat# CRL-3216
HEK293S cells	PMID: 25182477	N/A
ExpiCHO-S™ cells	Gibco	Cat# A29127
Experimental Models: Organisms/Strains		
Llama	VIB Nanobody Core	Chip No. 967000009804581
Pichia pastoris: strain GS115	Invitrogen	Cat# C18100
Oligonucleotides		
MP057 primer: 5'-TTATGCTTCCGGCTCGTATG-3'	This manuscript	N/A
Primers for cloning the VHHs in the pKai61 vector: 5'GGCGGGTATCTCTCGAGAAAAGGCAGGTGCAGCTGCAGGAGTCTGGG-3' 5'CTAACTAGTCTAGTGATGGTGATGGTGGTGGCTGGAGACGGTGACCTGG-3'	This manuscript	N/A
Primers for generation of bivalent VHH-constructs: 5'GGGGTATCTCTCGAGAAAAGGCAGGTGCAGCTGGTGGAGTCTGGG-3' 5'AGACTCCTGCAGCTGCACCTGACTACCGCCGCCTCCAGATCCACCTCCGCCACTACCGCCTCCGCCGCTGGAGACGGTGACCTGGG-3'	This manuscript	N/A
Recombinant DNA		

pCG1-SARS-2-S	PMID: 32142651	N/A
pCG1-SARS-S	PMID: 24023659	N/A
pKai61 vector	PMID: 19671134	N/A
pαH expression plasmid	Jason McLellan Laboratory	N/A
pαH-SARS-CoV-1 S TM	This manuscript	N/A
pαH-SARS-CoV-2 S TM	This manuscript	N/A
pαH-SARS VHH-72	This manuscript	N/A
pαH-MER VHH-55	This manuscript	N/A
pαH-MERS-CoV RBD	PMID: 24179220	N/A
pαH-SARS-CoV-1 RBD	PMID: 32075877	N/A
pαH-WIV1-CoV RBD	This manuscript	N/A
pαH-SARS-CoV-2 RBD-SD1	PMID: 32075877	N/A
pαH-SARS-CoV-1 NTD	This manuscript	N/A
pαH-MERS-CoV NTD	PMID: 28807998	N/A
pαH-MERS-CoV S1	This manuscript	N/A
pαH-SARS-CoV-1 S-2P	PMID: 28807998	N/A
pαH-MERS-CoV S-2P	PMID: 28807998	N/A
pαH-SARS-CoV-2 S-2P	PMID: 32075877	N/A
pαH-ACE2	PMID: 30356097	N/A
pαH-DPP4	PMID: 28807998	N/A
pHR′ CMV-Luc	Barney Graham Laboratory	N/A
CMV/R-MERS-CoV S	Barney Graham Laboratory	N/A
CMV/R-SARS-CoV-1 S	Barney Graham Laboratory	N/A
Software and Algorithms		
Flowing Software	http://flowingsoftware.btk.fi/	V2.5.1
Octet Data Analysis software	FortéBio	v11.1
GraphPad Prism	Motulsky et al., 2006	V7.0.4
Biacore X100 Evaluation Software	GE Healthcare	V2.0.1
iMOSFLM	Battye et al., 2011	https;//www.mrc-lmb.cam.ac.uk/harry/imosflm/ver721/downloads.html
Aimless	Evans and Murshudov, 2013	www.ccp4.ac.uk/download/
Phaser	McCoy et al., 2007	www.ccp4.ac.uk/download/
COOT	Emsley and Cowtan, 2004	http://bernhardcl.github.io/coot/
Phenix	Adams et al., 2002; Afonine et al., 2018	https://www.phenix-online.org/
ISOLDE	Croll, 2018	http://preview.cgl.ucsf.edu/chimerax/download.html
ChimeraX	Goddard et al., 2018	https://www.rbvi.ucsf.edu/chimerax/
Other		

Strep-Tactin Superflow resin	IBA Lifesciences	Cat# 2-1206-010
Pierce™ Protein A Agarose	ThermoFisher Scientific	Cat# 20334
Biacore X100 Sensorchip NTA	GE Healthcare	Cat# BR100407
HiLoad 16/600 Superdex75	GE Healthcare	Cat# 28989333
Superose6 XK 16/70	GE Healthcare	Cat# 90100042

Figure 1

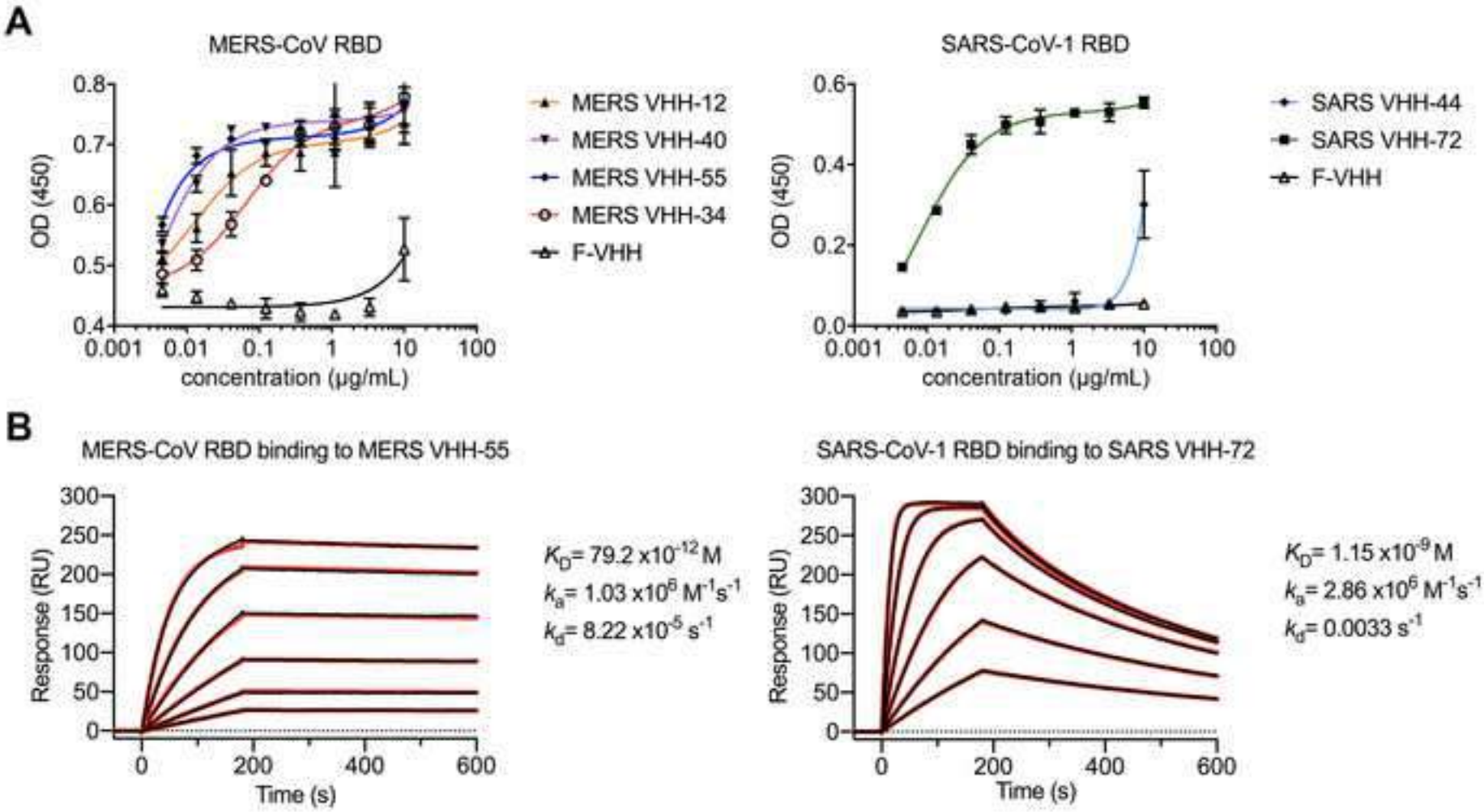

Figure 2

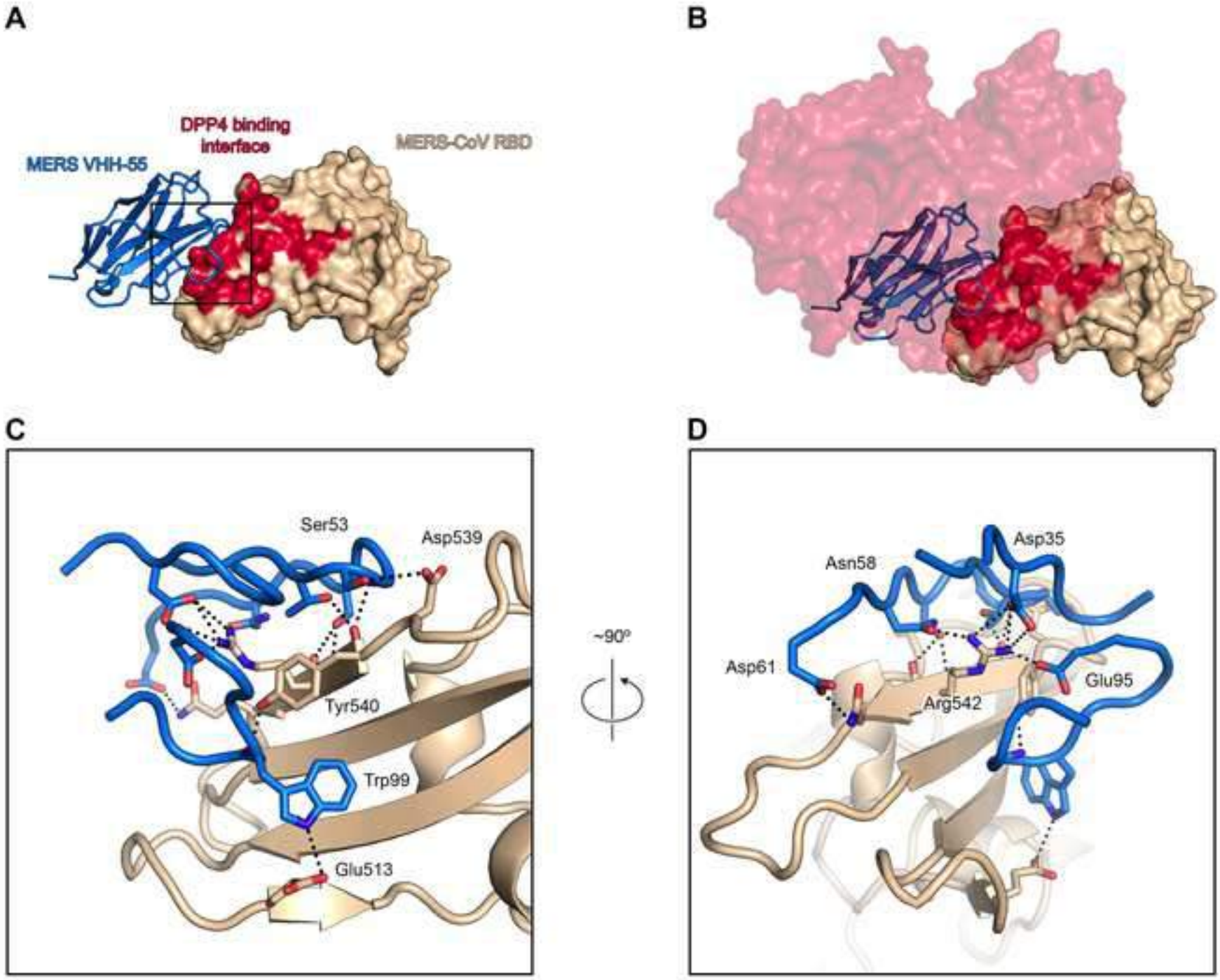

Figure 3

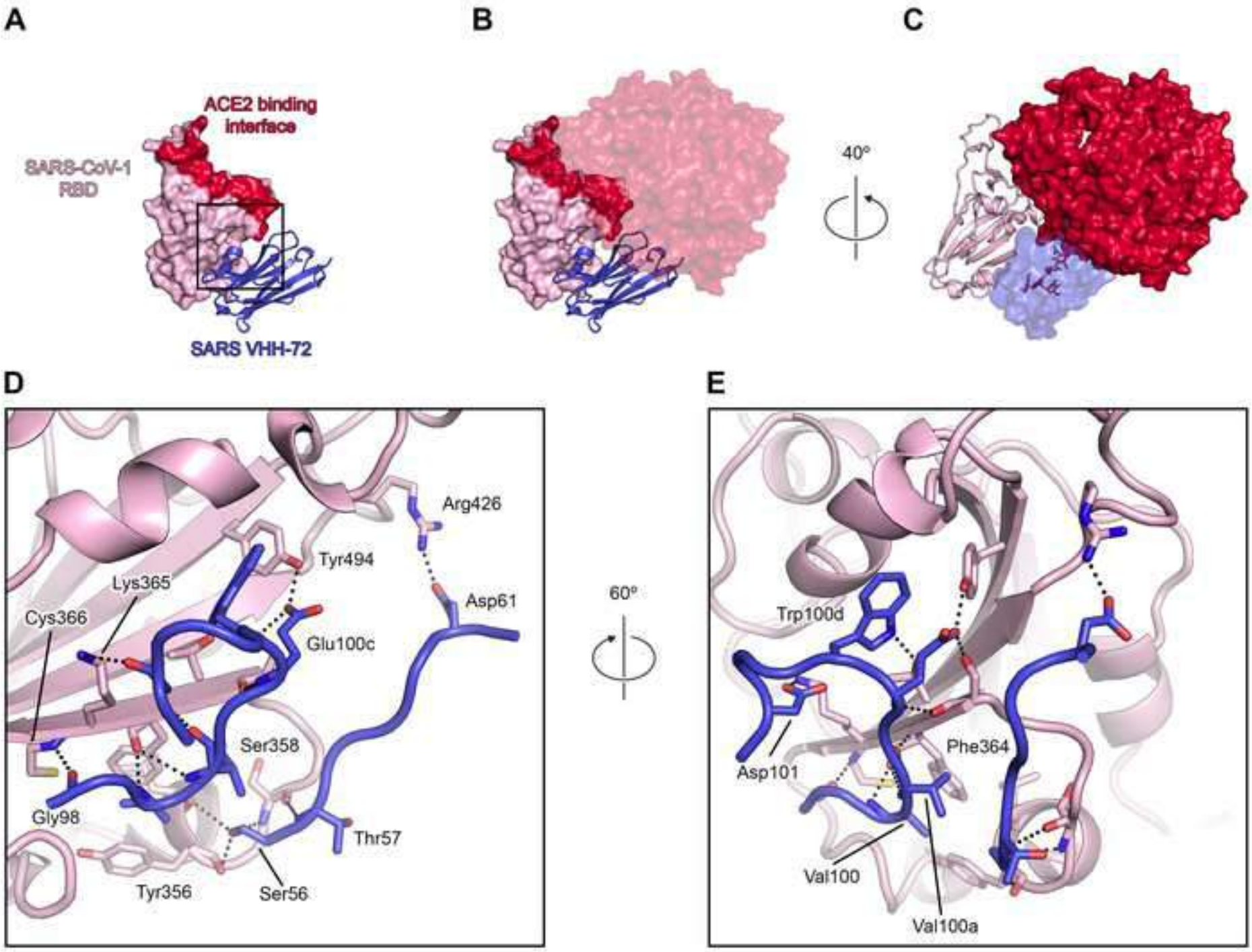

Figure 4

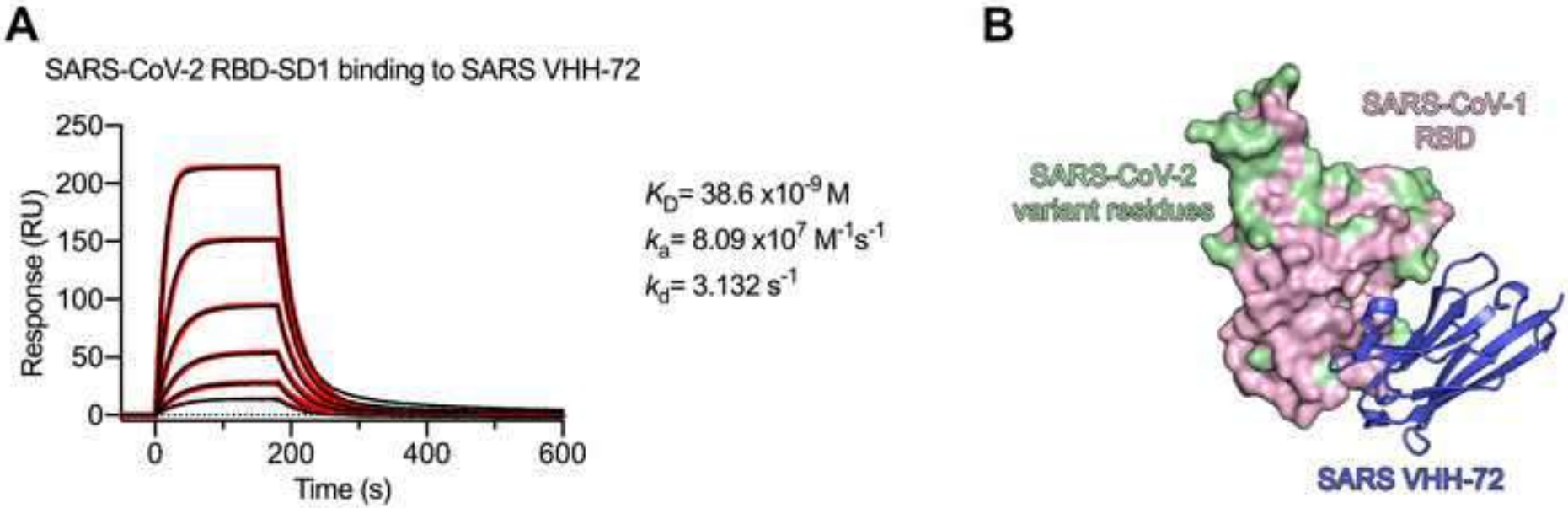

Figure 5

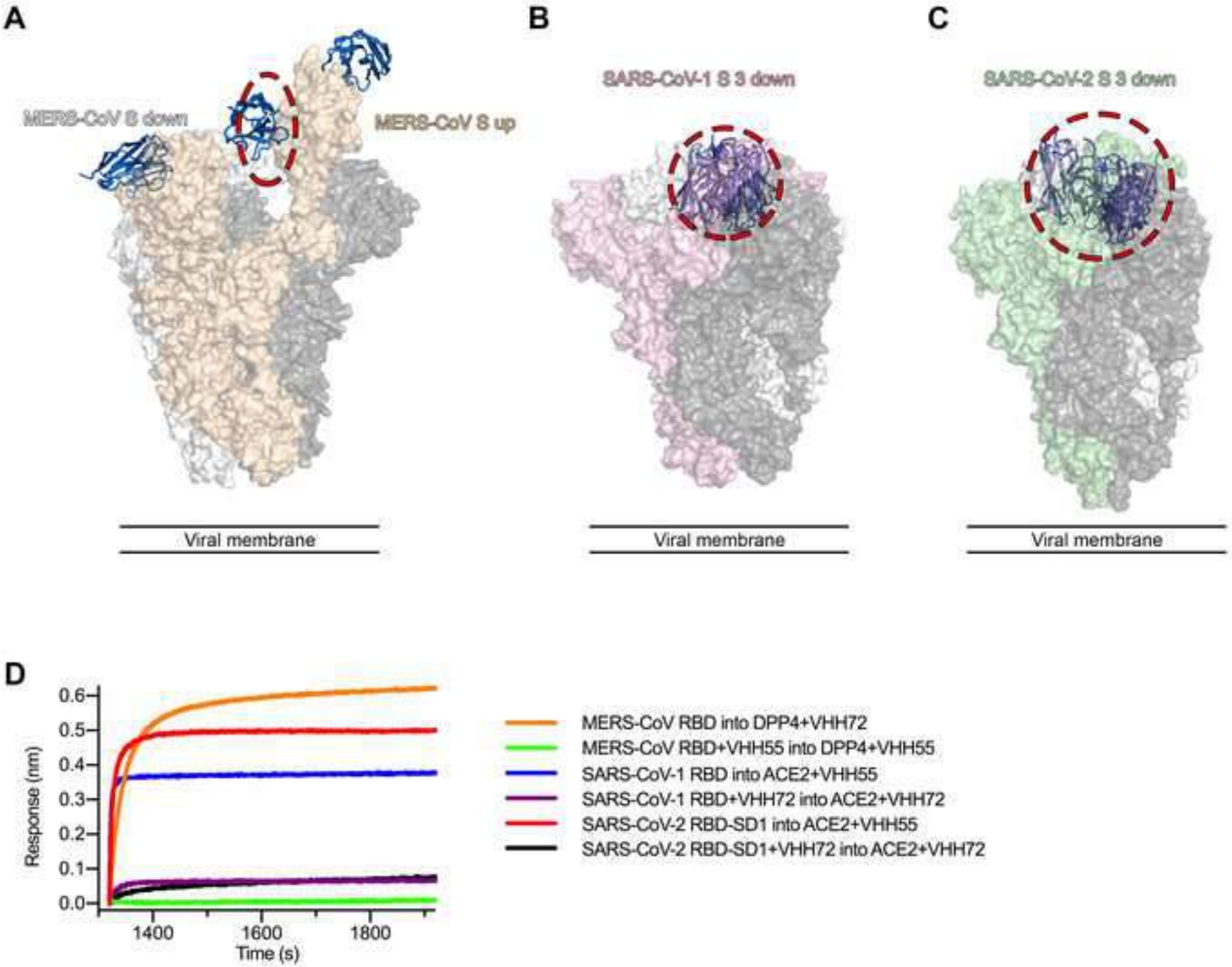

Figure 6

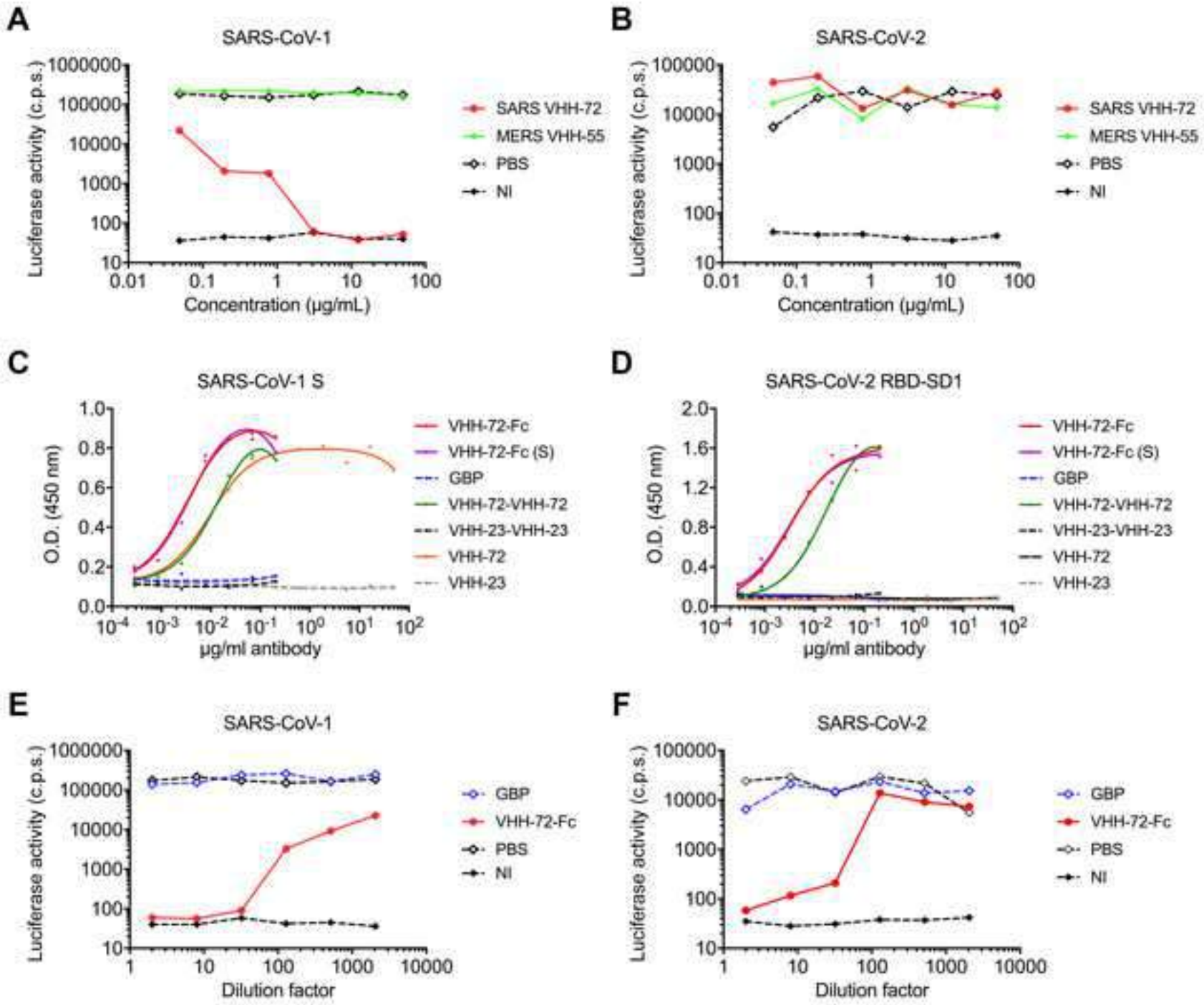

Figure 7

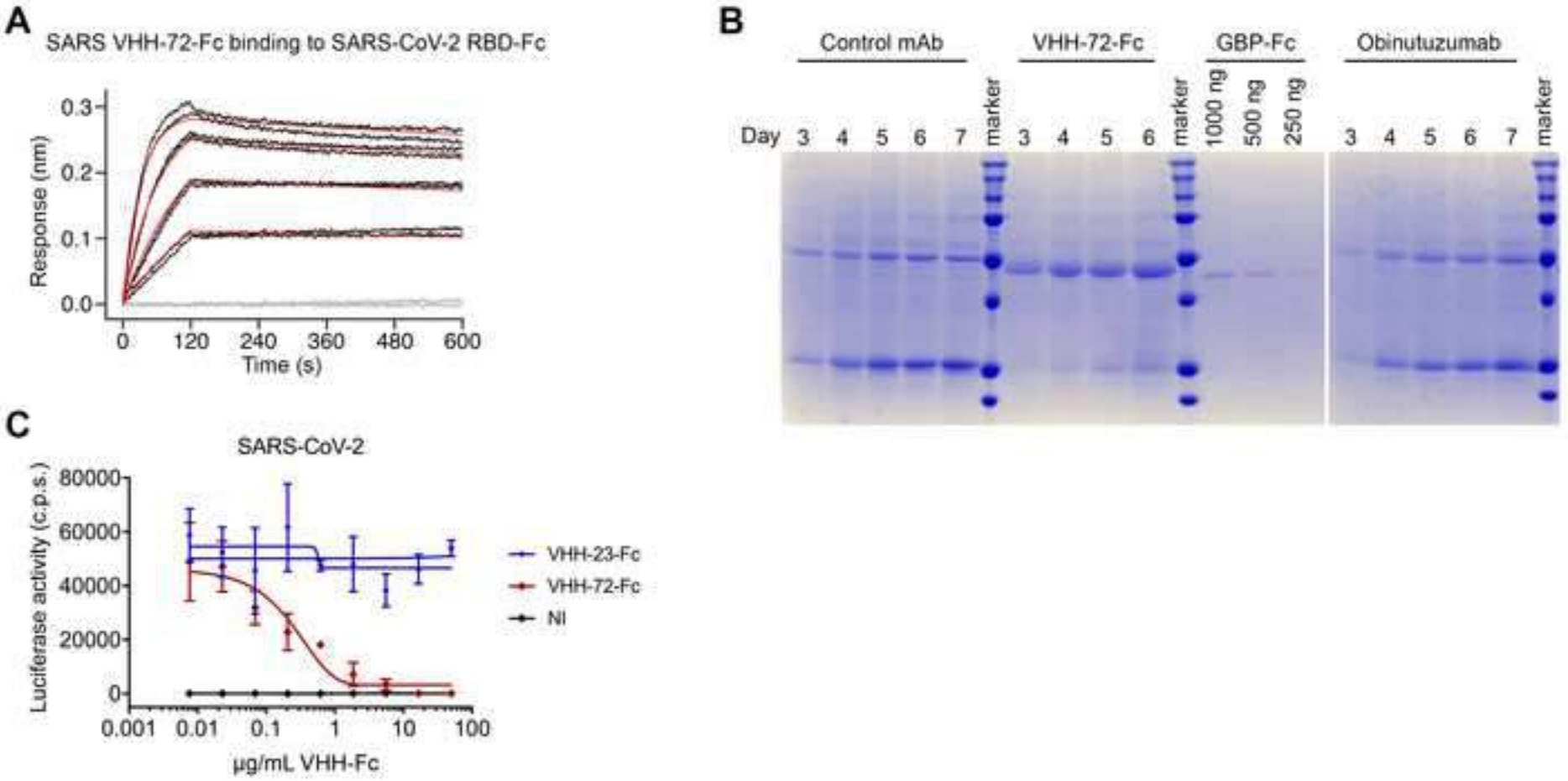

	Neutralization IC_{50}(μg/mL)	
	MERS-CoV England 1	SARS-CoV-1 Urbani
D12 mAb (ctrl)	0.01996	>10
MERS VHH-2	>10	>10
MERS VHH-12	0.13	>10
MERS VHH-15	>10	>10
MERS VHH-20	>10	>10
MERS VHH-34	2.9	>10
MERS VHH-40	0.034	>10
MERS VHH-55	0.014	>10
SARS VHH-1	>10	>10
SARS VHH-6	>10	>10
SARS VHH-35	>10	>10
SARS VHH-44	>10	5.5
SARS VHH-72	>10	0.14

Supplementary Table 1: MERS-CoV and SARS-CoV-1 pseudovirus neutralization data. Related to Figure 1.

	VHH-72 + SARS-CoV-1 RBD	VHH-55 + MERS-CoV RBD
PDB ID	6WAQ	6WAR
Data collection		
Space group	$P3_121$	$C222_1$
Cell dimensions		
a, b, c (Å)	88.8, 88.8, 200.8	150.0, 283.3, 173.7
α, β, γ (°)	90, 90, 120	90, 90, 90
Resolution (Å)	43.39-2.20 (2.28-2.20)	66.30-3.40 (3.51-3.40)
Rmerge	0.179 (1.669)	0.999 (3.752)
I/σI	6.2 (1.5)	6.2 (2.1)
CC1/2	0.993 (0.865)	0.485 (0.161)
Completeness (%)	99.8 (99.9)	98.5 (95.7)
Redundancy	8.9 (9.1)	5.8 (5.1)
Refinement		
Rwork/Rfree (%)	20.3/23.6	21.4/26.8
No. atoms		
Protein	4,934	20,270
Glycan (NAG)	42	42
Water	102	0
Average B-factors	78.5	84.3
Protein	78.8	84.3
Ligands	92.5	115.7
R.m.s. deviations		
Bond lengths (Å)	0.01	0.007
Bond angles (°)	0.76	1.05
Ramachandran		
Favored (%)	95.8	97.1
Allowed (%)	4.2	2.5
Outliers (%)	0.0	0.4

Supplementary Table 2: X-ray crystallography data collection and refinement statistics. Related to Figures 2 and 3.

Supplemental Figure 1

Click here to access/download;Supplemental Figure;Supp_Figure1_v9.tif

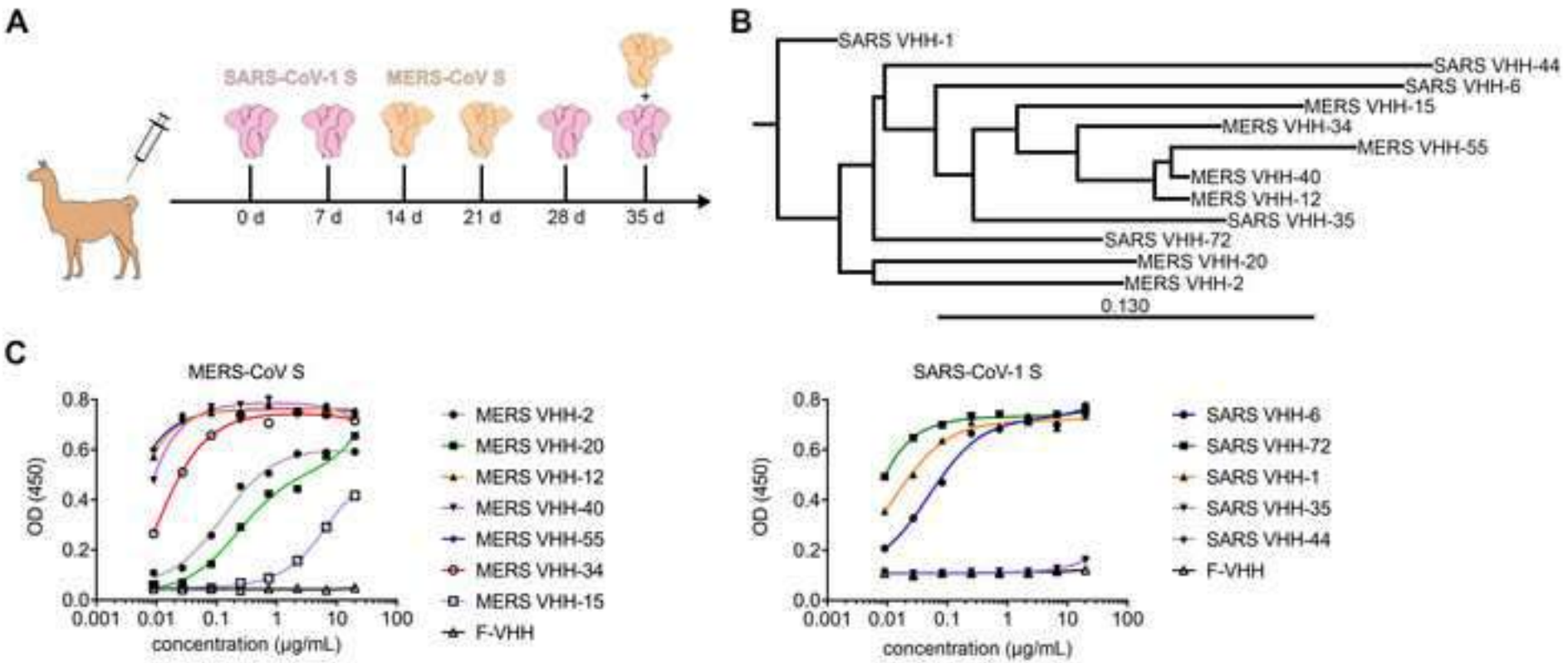

Supplemental Figure 2

Click here to access/download;Supplemental Figure;Supp_Figure2_v5.tif

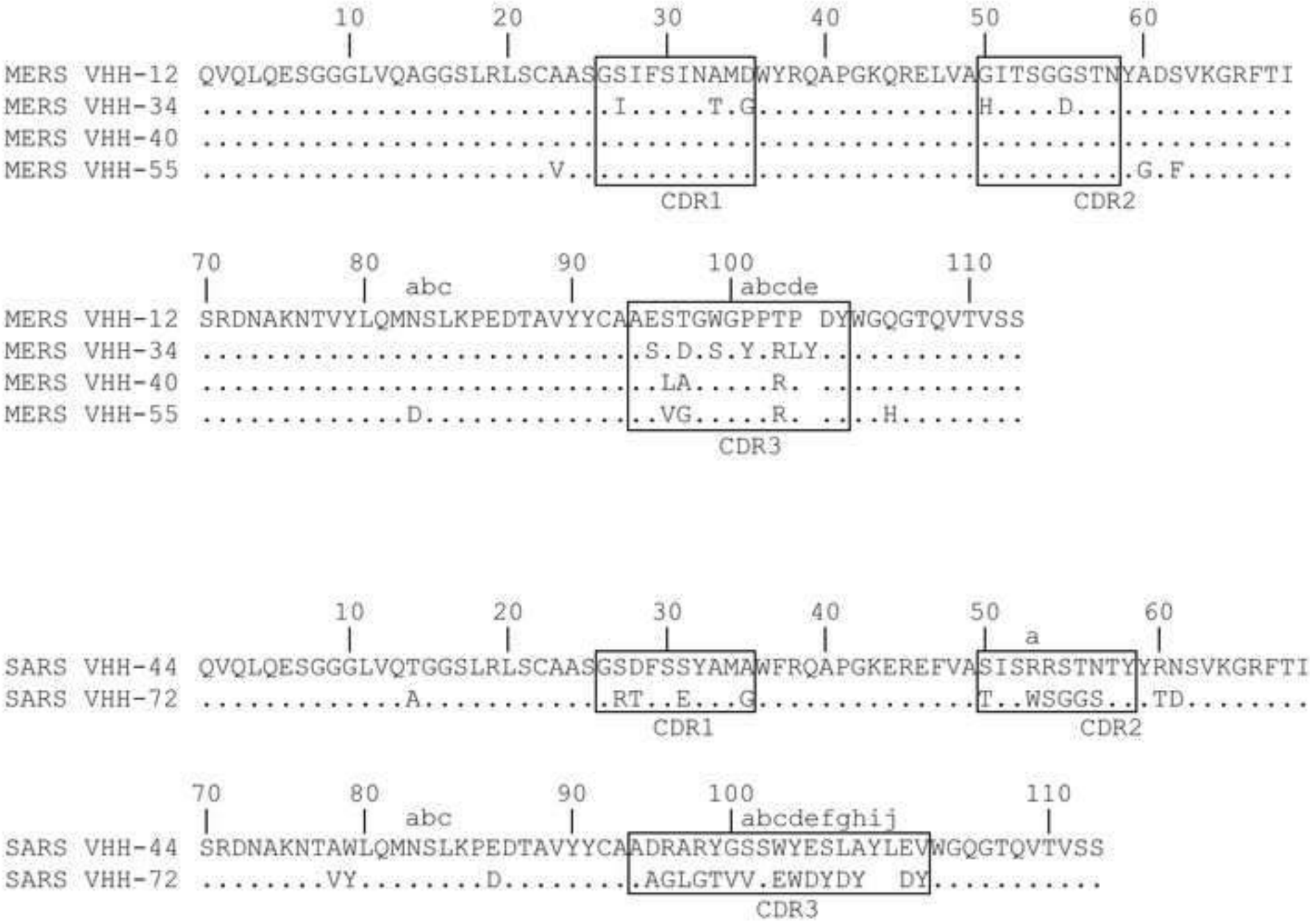

Supplemental Figure 3

Click here to access/download;Supplemental Figure;Supp_Figure3_v3.tif

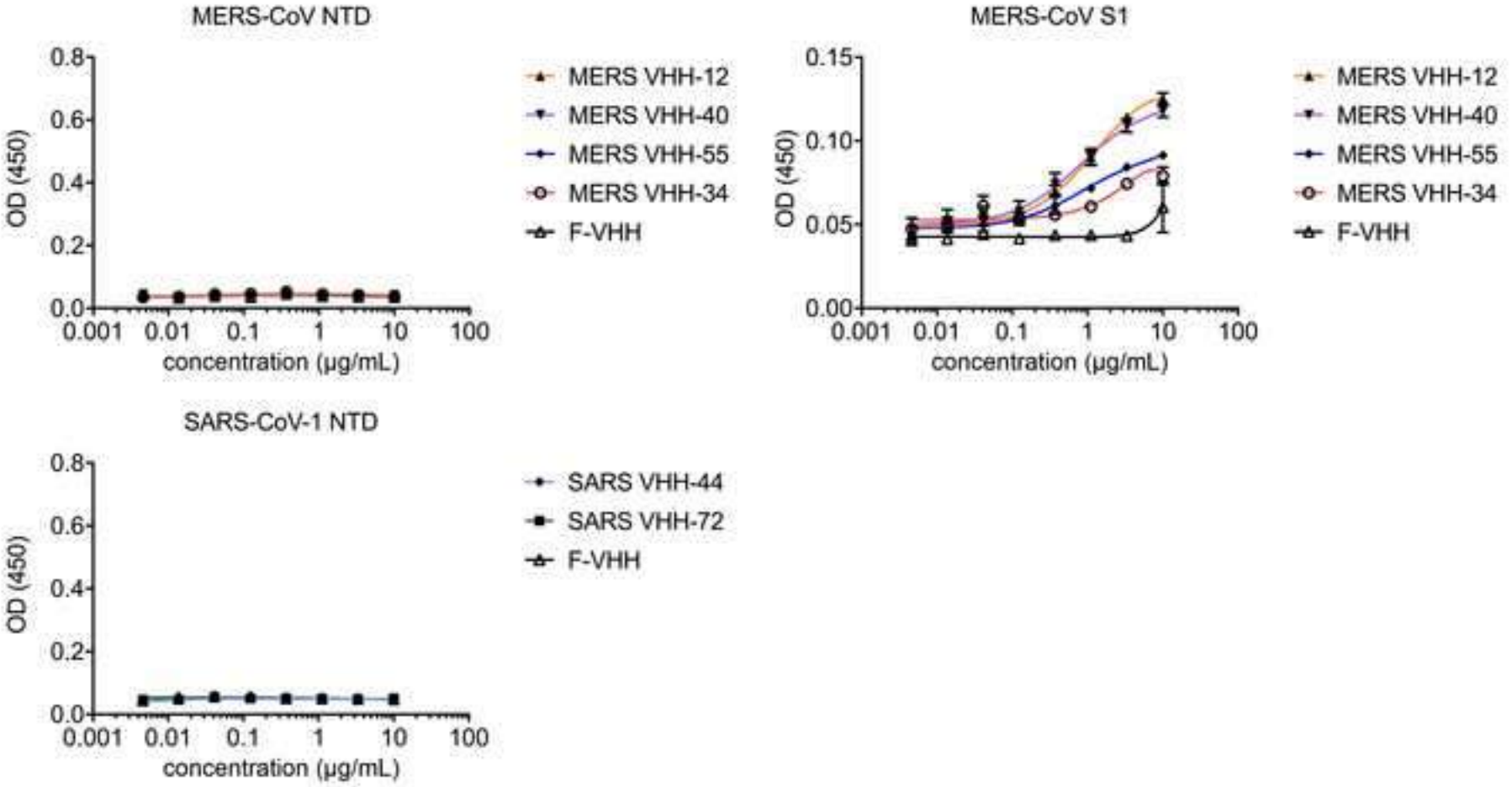

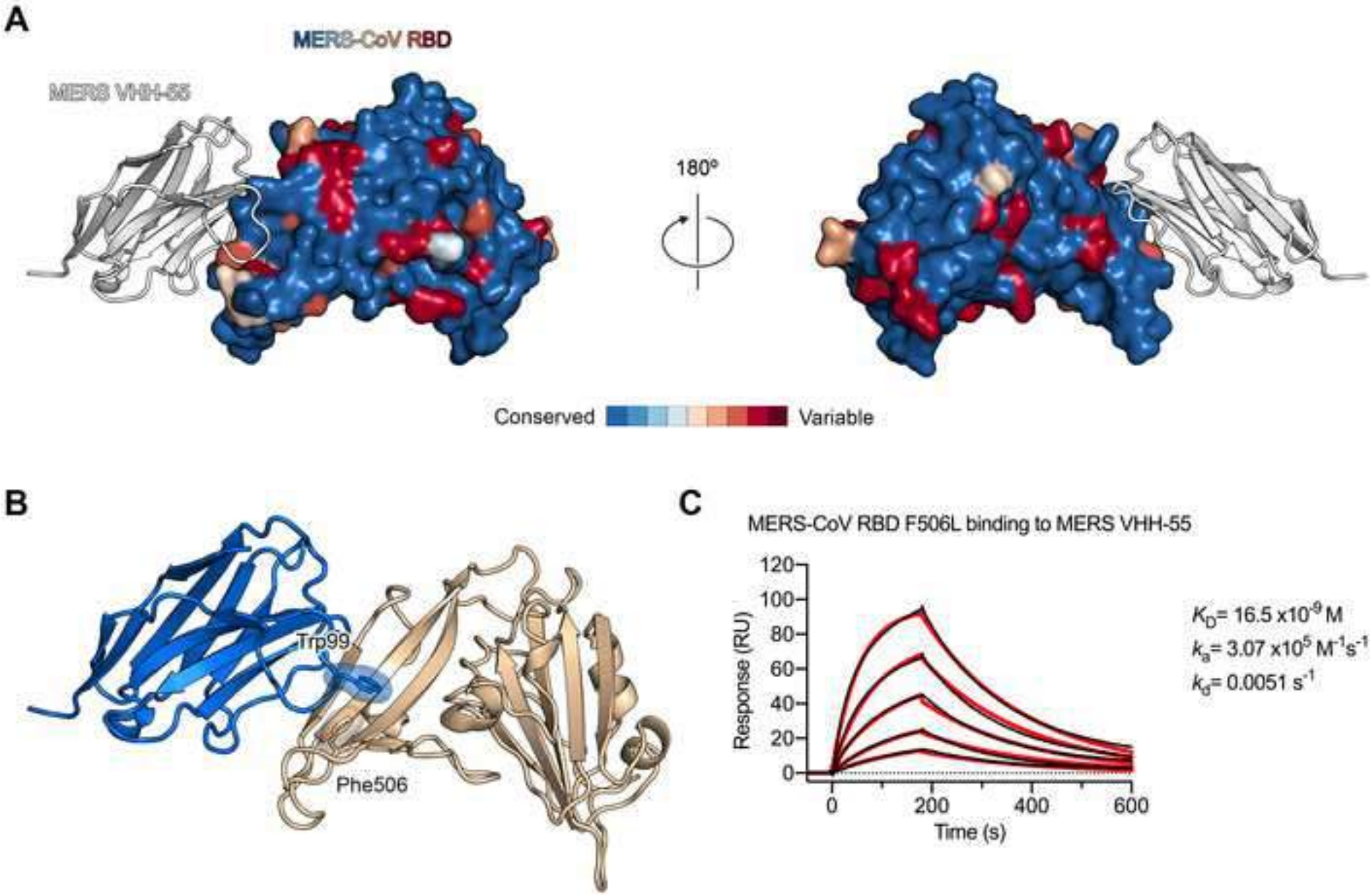

Supplemental Figure 5

Click here to access/download;Supplemental Figure;Supp_Figure5_v7.tif

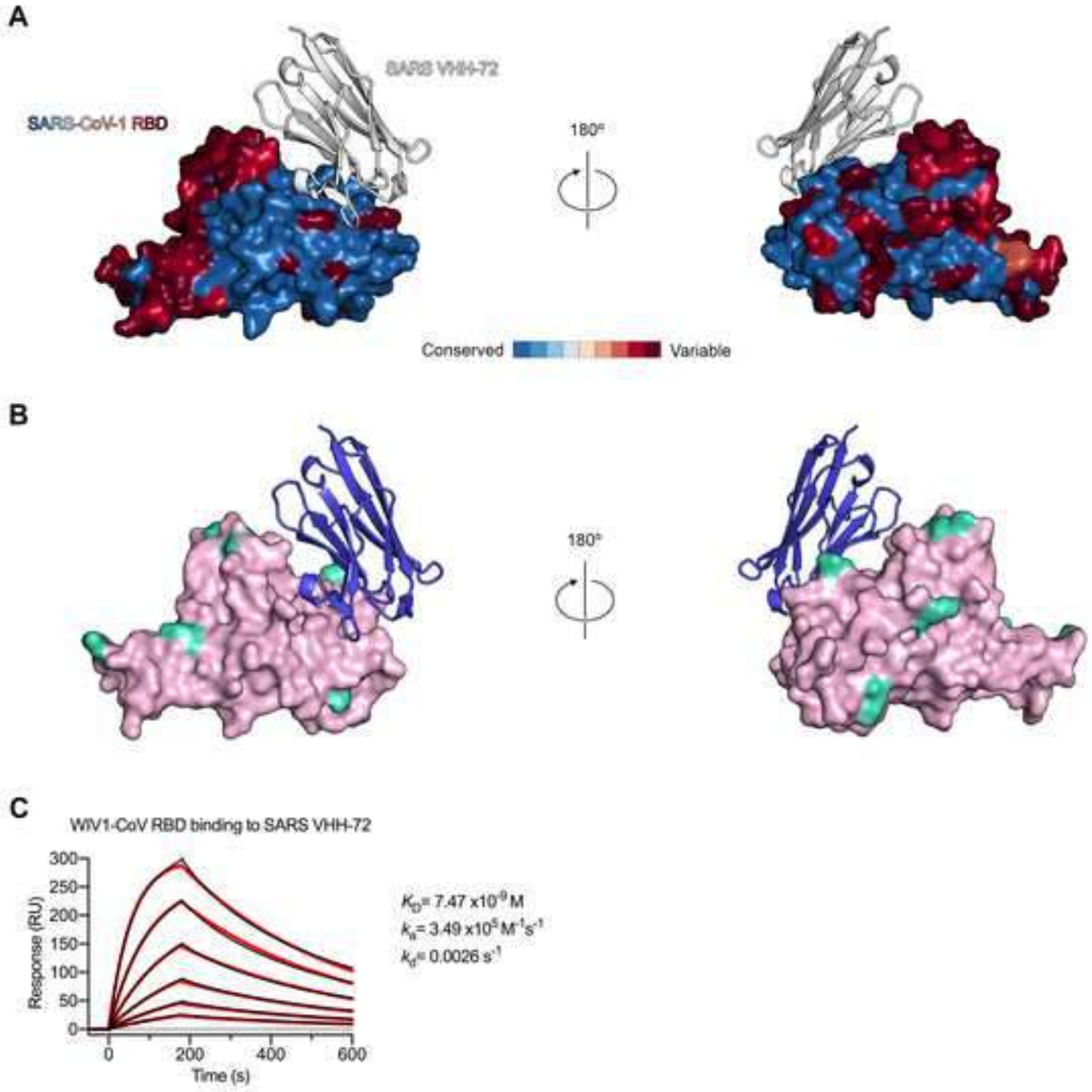

Supplemental Figure 6

Click here to access/download;Supplemental Figure;Supp_Figure6_v4.tif

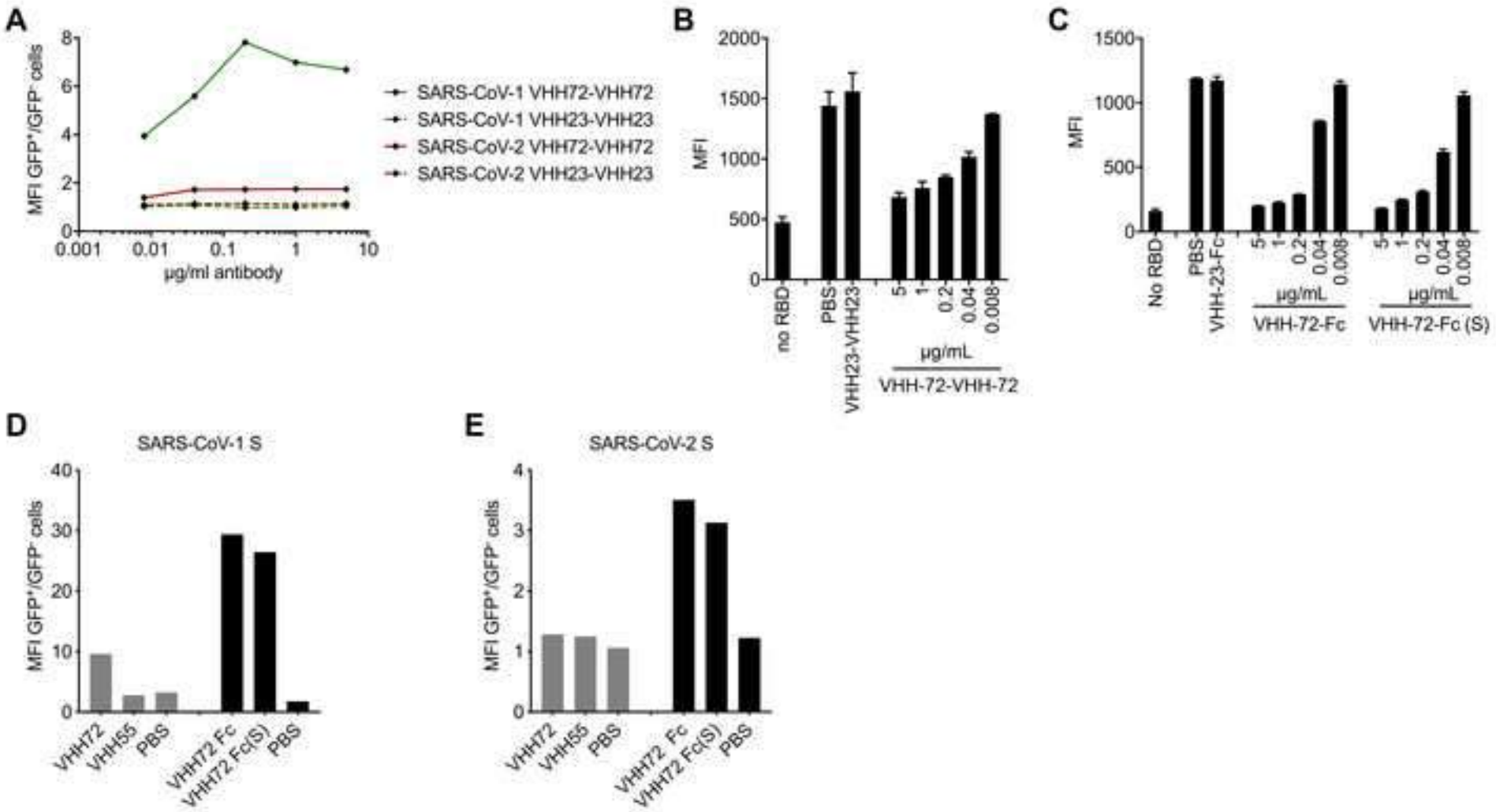

Supplemental Figure 7

Click here to access/download;Supplemental Figure;Supp_Figure7_v5.tif